J. Fluid Mech. (1993), *vol.* 250, *pp.* 433–480

Nonlinear evolution of waves on a vertically falling film

By H.-C. CHANG,[1] E. A. DEMEKHIN[2] AND D. I. KOPELEVICH[2]

[1] Department of Chemical Engineering, University of Notre Dame, Notre Dame, IN 46556, USA

[2] Department of Applied Mathematics, Krasnodar Polytechnical Institute, Krasnodar 350072, Russia

(Received 11 June 1992 and in revised form 25 November 1992)

Wave formation on a falling film is an intriguing hydrodynamic phenomenon involving transitions among a rich variety of spatial and temporal structures. Immediately beyond an inception region, short, near-sinusoidal capillary waves are observed. Further downstream, long, near-solitary waves with large tear-drop humps preceded by short, front-running capillary waves appear. Both kinds of waves evolve slowly downstream such that over about ten wavelengths, they resemble stationary waves which propagate at constant speeds and shapes. We exploit this quasi-steady property here to study wave evolution and selection on a vertically falling film. All finite-amplitude stationary waves with the same average thickness as the Nusselt flat film are constructed numerically from a boundary-layer approximation of the equations of motion. As is consistent with earlier near-critical analyses, two travelling wave families are found, each parameterized by the wavelength or the speed. One family γ_1 travels slower than infinitesimally small waves of the same wavelength while the other family γ_2 and its hybrids travel faster. Stability analyses of these waves involving three-dimensional disturbances of arbitrary wavelength indicate that there exists a unique nearly sinusoidal wave on the slow family γ_1 with wavenumber α_s (or α_2) that has the lowest growth rate. This wave is slightly shorter than the fastest growing linear mode with wavenumber α_m and approaches the wave on γ_1 with the highest flow rate at low Reynolds numbers. On the fast γ_2 family, however, multiple bands of near-solitary waves bounded below by α_f are found to be stable to two-dimensional disturbances. This multiplicity of stable bands can be interpreted as a result of favourable interaction among solitary-wave-like coherent structures to form a periodic train. (All waves are unstable to three-dimensional disturbances with small growth rates.) The suggested selection mechanism is consistent with literature data and our numerical experiments that indicate waves slow down immediately beyond inception as they approach the short capillary wave with wavenumber α_2 of the slow γ_1 family. They then approach the long stable waves on the γ_2 family further downstream and hence accelerate and develop into the unique solitary wave shapes, before they succumb to the slowly evolving transverse disturbances.

1. Introduction

Since the pioneering experiments of Kapitza (1948) and Kapitza & Kapitza (1949), the intricate wave structures that appear on the interface of a freely falling film have attracted considerable interest. By carefully controlling the amplitude and frequency of the imposed disturbances, they and many other subsequent experimentalists observed

that after a linear inception region where the fastest growing linear two-dimensional wave with wavenumber α_m is selectively amplified, the waves on a water film, for example, evolve downstream first into short periodic, nearly sinusoidal waves about 1 cm in length and then into very long 'solitary' waves which are more than 4 cm long. The latter waves typically consist of large tear-drop humps with steep downstream edges which are preceded by small, short capillary 'bow' waves. These solitary waves break up into three-dimensional waves further downstream. If the inlet flow rate is periodically forced at large amplitude and low frequency, the near-sinusoidal and solitary waves can be observed immediately without an inception region. These two-dimensional waves also seem to persist for long distance downstream (Nakoryakov, Pokusaev & Radev 1985). If, on the other hand, the disturbances are not properly controlled, the interface may break up into spatially and temporally irregular three-dimensional waves with pronounced transverse variation without exhibiting the sinusoidal and solitary two-dimensional waves. This typically occurs when three-dimensional disturbances are not suppressed at the inlet. In all the experiments which yielded two-dimensional waves, they are observed to evolve slowly downstream such that over a region of approximately 10 wavelengths, they do not change their shape or speed appreciably (see Kapitza's photograph in figure 11 for his 17 cm column). In contrast, three-dimensional waves tend to be non-stationary. This suggests that one can model the local two-dimensional waves as stationary waves which propagate at constant speed without changing their shapes. Another unique feature of two-dimensional waves which evolve through all three (inception, sinusoidal and solitary) wave regimes was first pointed out by Stainthorp & Allen (1965). The waves tend to decelerate as they enter the nearly sinusoidal range from the inception region and accelerate as their wavelength increases downstream towards the solitary wave limit.

Linear stability theory for falling films pioneered by Benjamin (1957) and Yih (1963), began soon after the first experiments were carried out. With modern computers, the solution of the Orr–Sommerfield equation for this problem is now complete. However, it was clear even at an early stage that wave evolution on a falling film is an extremely nonlinear phenomenon that cannot be described by a linear theory. The linear results and existing experimental data demonstrated that, even for a well-controlled experiment with water, an arbitrary small wave will increase its amplitude ten-fold according to the linear theory after an inception region of approximately 30 film thicknesses. Long before this, nonlinearity has already begun to manifest itself and saturate the exponential linear wave growth in the inception region. The saturated finite-amplitude waves evolve downstream, in the quasi-stationary manner described earlier, from sinusoidal waves to solitary waves before breaking up into non-stationary three-dimensional patterns. This quasi-stationary evolution of the waves suggests that if one can construct all stationary waves on the falling film and analyse their stability, the most stable or, more accurately, least unstable waves among these would then be the selected ones. This approach has also been applied to many other hydrodynamic phenomena such as Poiseuille flow (Pugh & Saffman 1988). Because of the extreme complexity of the full Navier–Stokes equation with nonlinear free-surface boundary conditions, most nonlinear studies have been based on the long-wave lubrication approximation (Lin 1974; Nakaya 1975) at low Reynolds numbers, $R \sim O(1)$. With this approximation, the Navier–Stokes equation reduces to a single partial differential equation commonly known as the evolution equation for the interface h. These evolution equations are highly nonlinear in h. If one carries out an expansion in h and stipulates a relative order between the two expansion parameters, the inverse wavelength and the wave amplitude, one can simplify the strongly nonlinear evolution

equations into weakly nonlinear ones like the Burgers' equation and the KdV equation for negligible surface tension (Benney 1966). For the case of strong surface tension and for amplitudes the same order as wavenumbers, a weakly nonlinear evolution equation which is now known as the Kuramoto–Sivashinsky equation results (Lin 1974; Shkadov 1973). These weakly nonlinear equations then allow the first estimates of the amplitude and speed of the near-sinusoidal stationary waves immediately beyond the inception region via the classical normal mode expansion of the Stuart–Landau formalism. This was carried out by Benney (1966), Gjevik (1970), Nakaya (1975), Tougou (1981), Chang (1989) and Lin (1974) who even carried out a sideband stability analysis of the sinusoidal waves by deriving a complex Ginzburg–Landau equation. A family of stationary waves with wavenumbers ranging from the neutral wavenumber α_0 to zero and with speed lower than the critical speed (three times the average velocity) are found. Since such a normal mode expansion preassumes that the waves contain only a few discrete Fourier harmonics, typically the unstable fundamental α and its stable overtone 2α for some wavenumber α near α_m, it can at best describe only the nearly sinusoidal waves near α_0. (For a more modern and systematic description of the Stuart–Landau theory using Center Manifold theory, see Cheng & Chang 1990 and Fujimura 1991.) Whenever the overtone 2α becomes linearly unstable, the Stuart–Landau equation with only one wave amplitude becomes invalid. Moreover, the Stuart–Landau equation neglects the subharmonic mode $\frac{1}{2}\alpha$ which is assumed to be linearly stable. If $\frac{1}{2}\alpha$ is linearly unstable, nonlinear waves described by the Stuart–Landau equation are often destabilized by subharmonic disturbances (Cheng & Chang 1992*b*) and undergoes a bifurcation to yield a new wave with significant subharmonic content. Since $2\alpha_m$ for a falling film becomes unstable soon after critically and $\frac{1}{2}\alpha_m$ is always unstable, the normal mode expansion theory resulting in a single amplitude equation for the fundamental is quite limited in its application. It is probably only appropriate for near-sinusoidal waves close to the critical Reynolds number or short waves near the neutral curve (Prokopiou, Cheng & Chang 1991). The weakly nonlinear equation itself, however, remains valid for all small-amplitude waves at low R. It is then possible that small stationary waves with a large Fourier mode content, that escape the classical Stuart–Landau normal mode expansion, still exist. This was first confirmed by Tsvelodub (1980), Demekhin (1983) and Demekhin & Shkadov (1986) who demonstrated numerically that the Kuramoto–Sivashinsky (KS) equation possesses other stationary waves with large Fourier content. They are actually an infinite number of stationary wave families, each parameterized by the wavelength. One family begins with the short, nearly sinusoidal waves with wavenumbers close to the neutral one. These are the ones estimated by earlier investigators using normal mode expansion. Subsequent wave members, however, increase their mode content rapidly, culminating at a solitary wave termination that has an infinitely broad Fourier band. These waves resemble the waves observed in the solitary regime with the unique tear-drop hump and the front-running capillary waves. Chang (1986) obtained an analytical estimate of the correlation between the speed c normalized with respect to the average velocity and the dimensionless amplitude h of all solitary waves, $h-1 = \pm\frac{1}{2}(c-3)$, via a normal form analysis. The two signs on the correlation reflect his discovery that two major families of waves, not one, have speeds c close to the critical speed, which is three times the average velocity. The near-sinusoidal members of the slow family γ_1 are the ones estimated by the Stuart–Landau formalism, which is essentially a Hopf bifurcation analysis near the neutral wavenumber α_0 where γ_1 bifurcates off the Nusselt flat-film basic state. The fast family γ_2 arises due to a unique characteristic of the falling film which yields an additional flat-

film basic state, the 'conjugate' solution. The γ_2 family bifurcates off this other basic state as we shall demonstrate later. Chang was able to resolve both families of waves by using a high-order bifurcation theory which includes the simple bifurcation due to the interaction of the two flat-film basic states and the two Hopf bifurcations corresponding to the creation of the two wave families from the two basic states. Homoclinic bifurcations of the two families of waves, corresponding to solitary waves, are also found for conditions near criticality ($R \to 0$). These provide the amplitude–speed correlation above. Chang demonstrated that the correlations are favourably compared to wave data in the solitary wave regime if the waves are small and R is of $O(1)$, namely where the KS equation is valid. For larger waves, one has to resort to the strongly nonlinear evolution equations. Chang (1989) carried out a higher-order amplitude expansion of the strongly nonlinear evolution equation for weak surface tension and also uncovered two families of travelling waves near the critical Reynolds number $R_c = 0$ for a vertical film. Like the KS equation for strong surface tension, both culminate in solitary waves with one family travelling faster than the critical phase speed that is three times the average velocity (twice the interfacial velocity) and one slower. With this higher-amplitude resolution for weak surface tension, the speed–amplitude correlation from the KS equation, $h-1 = \pm\frac{1}{2}(c-3)$, which applied to both solitary and shock waves in the KS limit, becomes only valid for shock waves. The solitary wave correlation now becomes $h = \pm\frac{3}{4}(c-3)$ near criticality. The stationary waves constructed in the above theory for $R \sim O(1)$ are in good agreement with experimental data. However, the stability of these waves, which should determine how the interface evolves downstream from one stationary wave to another, remains unresolved, although Pumir, Manneville & Pomeau (1983) and Joo, Davis & Bankoff (1991) have performed some numerical experiments concerning the time evolution of periodic waves for strongly nonlinear evolution equations.

For the practically more important conditions of high Reynolds numbers, the only reported constructions of nonlinear stationary waves are based on a drastic *ad hoc* averaging approximation which assumes that the velocity profile is locally either flat for turbulent films or parabolic for laminar ones at every location. This yields an evolution equation, known as the averaged equation, for both the interface h and the local flow rate q. This simplifying approach was first introduced by Kapitza (1948) and some stationary waves, including near-sinusoidal and solitary ones, have been constructed by Shkadov (1967, 1968), Demekhin & Shkadov (1985), Hwang & Chang (1987), Prokopiou *et al.* (1991) and Trifonov & Tsvelodub (1991). Hwang & Chang and Prokopiou *et al.* demonstrate that the wave speeds of the solitary waves under turbulent and laminar conditions, respectively, are accurately estimated with this approximate theory. At large R, the equation again yields two solitary waves, the slower one travelling at 1.67 times the average liquid velocity. Each solitary wave is the termination point of a fast and a slow family of waves, quite reminiscent of the two families constructed analytically by Chang (1986, 1989) for thin films with $R \sim O(1)$. Prokopiou *et al.* (1991) have also used this equation to show that near-sinusoidal waves of the slow family are unstable to disturbances twice their wavelength (subharmonic instability). This is consistent with Brauner & Maron's (1983) observation that the waves tend to double their wavelength as they evolve from the sinusoidal region into the solitary region. Unfortunately, the amplitude and shape of the constructed waves do not resemble the observed ones at high R (see figure 5 of Prokopiou *et al.*). This then suggests that the averaging approximation may erase many stationary waves, including the observed ones, even though it provides a good prediction of the solitary wave speed. The evolution of stationary waves downstream may then be beyond the

description of the averaged equation and even the subharmonic mechanism suggested by Prokopiou *et al.* is in doubt. It would hence be extremely desirable to remove the averaging simplification. We shall show here that the averaged equation is only valid at low Reynolds number ($R < 10$ for water). Bach & Villadsen (1984), Kheshgi & Scriven (1987) and Ho & Patera (1990) have integrated the full Navier–Stokes equation in time and obtained at large time stationary solitary waves and sinusoidal waves that resemble the observed ones. However, a complete classification of all stationary waves at high Reynolds number and their evolution and competition have not been reported. We carry out such an analysis here with only a long-wave boundary-layer approximation and report the first satisfactory comparison to observed waves of all three regimes at high R. We also link the waves at high Reynolds number to the waves of the KS equation at low R. Basically, the two families of waves, γ_1 and γ_2, persist with some modification at high R although the fast family breaks into several hybrid ones with distinctive shapes. The observed nearly sinusoidal waves belong to the slow family and the solitary ones the fast family. We also carry out a linear stability analysis of the stationary waves with respect to three-dimensional disturbances of all wavelengths. Subharmonic instability of near-sinusoidal waves is confirmed. However, other dominant long-wave instabilities are also discovered. One wave member on γ_1 and a finite number on γ_2 are found to yield local minima in the growth rate and are hence the selected quasi-stationary waves. The physical mechanisms for selecting these waves are explored. We also construct an evolution scenario linking these selected waves which explains the initial deceleration and subsequent acceleration observed by Stainthorp & Allen (1965). In §2, we derive the boundary-layer equation from the equations of motion and carry out a simple linear stability analysis that yields results close to those from the complete Orr–Sommerfeld equation. Some analytical results can be derived because of the boundary-layer approximation. In §3, we report a most complete tracing of all stationary wave families and solitary waves of the KS equation which is the limiting version of our equation. In §4, we construct and characterize all stationary wave solutions of the boundary-layer equation beginning from the KS waves and compare them to reported wave tracings. A three-dimensional linear stability of the constructed waves and their physical interpretation are contained in §5. The predicted evolution scenario is satisfactory compared to literature data and a numerical evolution experiment. A summary is offered in §6.

2. Boundary-layer equations and linear stability

We consider a viscous fluid layer falling freely down an inclined plane with an inclination angle θ under the influence of gravity. The waveless flat film has a thickness h_N, the Nusselt film thickness, which is related to the mean velocity $\langle u \rangle$, sometimes known as the Nusselt velocity, of the parabolic profile by $\langle u \rangle = \frac{1}{3} g h_N^2 \sin\theta/\nu$. Using $\langle u \rangle$ as the characteristic velocity and h_N as the characteristic length, the dimensionless Navier–Stokes equation becomes

$$\frac{\partial \boldsymbol{u}}{\partial t} + \boldsymbol{u}\cdot\nabla\boldsymbol{u} = -\nabla p + \frac{1}{R}\nabla^2\boldsymbol{u} + \frac{3}{R}\boldsymbol{g}, \tag{1}$$

$$\nabla\cdot\boldsymbol{u} = 0, \tag{2}$$

where $\boldsymbol{u} = (u, v, w)$ is the velocity field, $R = \langle u \rangle h_N/\nu$ is the Reynolds number and $\boldsymbol{g} = (1, -\operatorname{cotan}\theta, 0)$. The coordinate system is chosen such that the upper normal of the inclined plane is y, x is along the downward tangent and z is in the transverse

	Mercury (20 °C) $\gamma = 28000$		H_2O (15 °C) $\gamma = 2850$		Glycerin (20 °C) $\gamma = 0.18$	
R	5δ	$\epsilon \times 10^{-4}$	5δ	$\epsilon \times 10^{-3}$	5δ	ϵ
1	0.014	1.2	0.030	0.54	0.755	0.341
5	0.100	2.4	0.214	1.10	5.390	0.697
10	0.233	3.3	0.501	1.51	12.57	0.948
50	1.670	6.7	3.580	3.12	89.85	1.939
100	3.900	9.1	8.350	4.21	209.7	2.638
500	27.881	18.7	59.72	8.53	1499.3	5.395
1000	65.04	25.0	139.3	12.0	3498.0	7.341

TABLE 1. Typical values of δ and ϵ for $\theta = \frac{1}{2}\pi$

direction. Let the free-surface position $f(x, t)$, where $x = (x, y, z)$ are the Cartesian coordinates, be defined by

$$f(x, t) = y - h(x, z, t) = 0, \tag{3}$$

and assuming the pressure in the gas phase remains at constant value p_0, one obtains the kinematic and stress conditions at the interface $y = h$:

$$\partial f/\partial t + \boldsymbol{u} \cdot \nabla f = 0, \tag{4a}$$

$$[p - p_0 - WK(h)]\, n_i - t_{ij} n_j = 0, \quad i,j = 1,2,3, \tag{4b}$$

where K is the curvature at the interface, t_{ij} is the shear tensor $1/R(\partial u_i/\partial x_j + \partial u_j/\partial x_i)$ and $W = \sigma/\rho\langle u\rangle^2 h_N$ is the Weber number. The unit vector $\boldsymbol{n}$ is normal to the free surface. There is also the no-slip condition at the wall

$$\boldsymbol{u} = \boldsymbol{0} \quad \text{at} \quad y = 0. \tag{5}$$

Equations (1)–(5) then define the full equations of motion for the falling-film problem. It is a problem with three dimensionless parameters: R, W and θ. It is popular among the Russian school to replace the Weber number by the Kapitza number $\gamma = \sigma/\rho\nu^{\frac{4}{3}}g^{\frac{1}{3}}$ which is only a function of the fluid properties and not the flow conditions. The Kapitza number can be expressed as

$$\gamma = WR^{\frac{5}{3}}/(3\sin\theta)^{\frac{1}{3}}. \tag{6}$$

It is extremely tedious to search for all solutions of the above equation in a three-dimensional parameter space. A considerable simplification can be achieved if we limit ourselves to $R < 500$ such that the characteristic wavelength, on the orders of centimetres, is much longer than h_N which is no more than 2 or 3 mm. In this limit, we can invoke the long-wave boundary-layer approximation which neglects $\partial/\partial x$ and $\partial/\partial z$ in favour of $\partial/\partial y$. The usual long-wave expansion with

$$v \to v/\kappa, \quad (x, z, t) \to \kappa(x, z, t)$$

can then be introduced, where κ is a large parameter relating the ratio of the x and z characteristic scale to the y scale. It is convenient to choose

$$\kappa^3 = \tfrac{1}{3}WR = \sigma/\rho g h_N^2 \sin\theta, \tag{7}$$

as Demekhin, Demekhin & Shkadov (1983). Hence, RW must be a large number but there is no stipulation on the relative magnitude of R or W. The case of $\kappa \gg 1$ studied here is commonly referred to as the strong surface tension case. It applies to water and

most other liquids but not glycerin for $\theta \gg 1$ (see table 1). Upon substitution, one obtains three new parameters: θ and

$$\delta = \frac{R}{15\kappa} = \frac{R^{\frac{11}{9}}}{5\gamma^{\frac{1}{3}}3^{\frac{7}{9}}}\sin\theta^{\frac{1}{9}}, \qquad \epsilon = \frac{1}{15\kappa^2} = \frac{3^{\frac{4}{9}}R^{\frac{4}{9}}}{15\gamma^{\frac{2}{3}}}\sin\theta^{\frac{2}{9}}. \tag{8a, b}$$

As shown in table 1, $\epsilon \ll 1$ for most fluids with $R < 500$. The exception lies with low surface tension fluids like glycerin that have ϵ small only for $R < 5$. We shall hence set ϵ to zero and effectively reduce the number of parameters by one. The final equation, which is derived in Appendix A, is then

$$\frac{\partial u}{\partial t}+u\frac{\partial u}{\partial x}+v\frac{\partial u}{\partial y} = \frac{1}{5\delta}\left(\frac{\partial^3 h}{\partial x^3}+\frac{1}{3}\frac{\partial^2 u}{\partial y^2}+1\right)-3\chi\frac{\partial h}{\partial x}, \tag{9a}$$

$$\frac{\partial u}{\partial x}+\frac{\partial v}{\partial y} = 0, \tag{9b}$$

$$y = h(x,t): \quad h_t = v-u\frac{\partial h}{\partial x}, \quad \frac{\partial u}{\partial y} = 0, \tag{9c, d}$$

$$y = 0: \quad u = v = 0 \tag{9e}$$

for the two-dimensional case where $\chi = \operatorname{cotan}\theta/R$. It is often convenient to replace the kinematic condition (9*c*) at the interface by the equivalent integral form

$$\frac{\partial h}{\partial t}+\frac{\partial}{\partial x}\int_0^h u\,\mathrm{d}y = 0. \tag{9f}$$

The three-dimensional version is

$$\frac{\partial u}{\partial t}+u\frac{\partial u}{\partial x}+v\frac{\partial u}{\partial y}+w\frac{\partial u}{\partial z} = \frac{1}{5\delta}\left(h_{xxx}+h_{xzz}+\frac{1}{3}\frac{\partial^2 u}{\partial y^2}+1\right)-3\chi\frac{\partial h}{\partial x}, \tag{10a}$$

$$\frac{\partial w}{\partial t}+u\frac{\partial w}{\partial x}+v\frac{\partial w}{\partial y}+w\frac{\partial w}{\partial z} = \frac{1}{5\delta}\left(h_{xxz}+h_{zzz}+\frac{1}{3}\frac{\partial^2 w}{\partial y^2}\right)-3\chi\frac{\partial h}{\partial z}, \tag{10b}$$

$$\frac{\partial u}{\partial x}+\frac{\partial v}{\partial y}+\frac{\partial w}{\partial z} = 0, \tag{10c}$$

$$y = h(x,z,t): \quad h_t = v-uh_x-wh_z, \quad \frac{\partial u}{\partial y} = \frac{\partial w}{\partial y} = 0, \tag{10d, e}$$

$$y = 0: \quad u = v = w = 0, \tag{10f}$$

and the three-dimensional analogue of (9*f*)

$$\frac{\partial h}{\partial t}+\frac{\partial}{\partial x}\int_0^h u\,\mathrm{d}y+\frac{\partial}{\partial z}\int_0^h w\,\mathrm{d}y = 0. \tag{10g}$$

In all subsequent studies, we shall examine only the case of a vertical plane $\chi = 0(\theta = \frac{1}{2}\pi)$ and hence the entire problem is conveniently parameterized by a single parameter δ.

We examine the validity of the boundary-layer equation by comparing its linear stability result for the Nusselt flat-film base state to those from the Orr–Sommerfeld equation of the linearized version of the Navier–Stokes equation. Because of the boundary-layer approximation, the linear stability of large $\alpha\delta$ can actually be studied

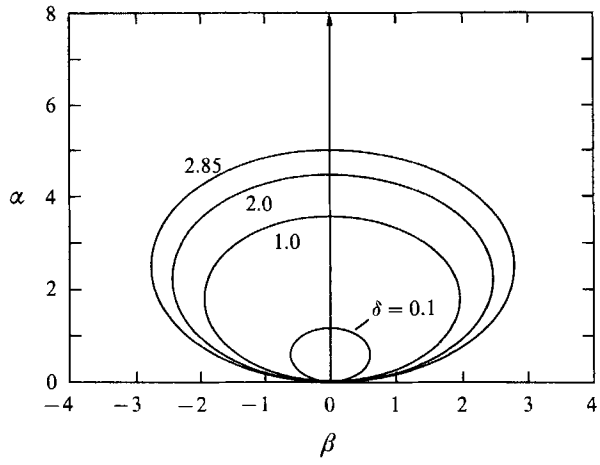

FIGURE 1. Neutral curves of the primary instability of the Nusselt flat film in the two-dimensional wavenumber space α, β. The most unstable wave is two-dimensional with $\beta = 0$.

analytically. This is because the outer equation, unlike the Rayleigh equation of the Orr–Sommerfeld equation, can now be solved in closed form. Linearizing (10) about the basic state $(U, V, W, h) = (3(y-\frac{1}{2}y^2), 0, 0, 1)$ and inserting a disturbance with a normal mode of $\exp[\mathrm{i}(\alpha x+\beta z-\alpha ct)]$, one obtains

$$\phi'''-15\mathrm{i}\alpha\delta[(U-c)\phi'-U'\phi] = -3\mathrm{i}(\alpha^2+\beta^2)^2/\alpha, \tag{11a}$$

$$y = 1: \quad \phi'' = -3, \quad \phi = \tfrac{3}{2}-c, \tag{11b}$$

$$y = 0: \quad \phi = \phi' = 0, \tag{11c}$$

where $\phi = -\mathrm{i}v/\alpha$ is the complex stream function.

For small $\alpha\delta$ at near-critical conditions ($\delta \to 0$), a routine expansion of (11) yields the expected results for the neutral curve

$$c_0 = 3, \tag{12a}$$

$$(\alpha^2+\beta^2)^2 = 18\alpha^2\delta, \tag{12b}$$

such that the neutral wavenumber for two-dimensional waves is

$$\alpha_0 = (18\delta)^{\frac{1}{2}}, \tag{12c}$$

and the most unstable disturbance is a two-dimensional one:

$$\alpha_{\mathrm{m}} = \frac{1}{\sqrt{2}}\alpha_0 = (9\delta)^{\frac{1}{2}}, \quad \beta_{\mathrm{m}} = 0. \tag{12d}$$

The critical condition for the vertical layer is then $\delta_{\mathrm{c}} = 0$. Equations (12*c*) and (12*d*) are in agreement with the standard long-wave expansion of the Orr–Sommerfeld equation by Yih (1963) and Benney (1966). The results for conditions far from criticality, $\alpha R \gg 1$, could only be obtained numerically because the Orr–Sommerfeld equation cannot be solved analytically even by matched asymptotic expansion. This is different for the boundary-layer equation and we offer a closed-form solution by solving the outer equation explicitly. For the inner region near the wall, the dominant terms of (11*a*) yield

$$\phi \sim -\frac{(\alpha^2+\beta^2)^2}{5\alpha^2 c\delta}y + A_0\,\mathrm{e}^{(-1+\mathrm{i})\mu y} - A_0, \tag{13}$$

		Orr–Sommerfeld (Pierson & Whitaker)		Boundary layer	
R	δ	α_m	αc_i^{max}	α_m	αc_i^{max}
0.667	0.00345	0.1676	0.8388×10^{-3}	0.1762	0.9639×10^{-3}
3.333	0.0247	0.4503	0.0418	0.4646	0.04631
6.667	0.0575	0.6337	0.1487	0.6426	0.1614
33.33	0.411	0.7727	0.2365	0.8060	0.2418
66.67	0.97	0.8432	0.1769	0.8711	0.1784
333.33	6.88	1.0627	0.07558	1.1628	0.07596
666.66	16.0	1.2079	0.05161	1.2581	0.05159

TABLE 2. Linear stability for water ($\gamma = 2850$)

where $\mu = (\frac{15}{2}\alpha c\delta)^{\frac{1}{3}}$ and A_0 is determined to be $-(\alpha^2+\beta^2)^2(1+\mathrm{i})/10\,\alpha^2 c\delta\mu$. The inner region near the free surface can likewise be resolved to be

$$\phi \sim A_1 - \frac{(\alpha^2+\beta^2)^2}{5\alpha^2(c-\frac{3}{2})\delta}(y-1) + A_2 \mathrm{e}^{(1-\mathrm{i})\eta(y-1)}, \tag{14}$$

where $\eta = [\frac{15}{2}\alpha(c-\frac{3}{2})\delta]^{\frac{1}{3}}$ and A_2 is determined from (11*b*) to be $-3\mathrm{i}/2\eta^2$ but A_1 remains unknown. The outer region away from the two boundary layers, unlike the Rayleigh equation of the Orr–Sommerfeld equation, is described by a first-order equation which can be easily integrated to yield

$$\Phi \sim \frac{(\alpha^2+\beta^2)^2}{5\alpha^2\delta}(U-c)\int_0^y \frac{\mathrm{d}y}{(U-c)^2} - \frac{(\alpha^2+\beta^2)^2}{10\alpha^2 c^2\delta\mu}(U-c)(1+\mathrm{i}). \tag{15}$$

Matching this to the inner solution at the interface, we obtain $A_1 = \Phi(1)$ and from (11*b*) we get the dispersion relationship

$$\frac{-(\alpha^2+\beta^2)^2}{10\alpha^2\delta}\left\{\frac{1}{c} + \frac{2}{(6c-9)^{\frac{1}{2}}}\arctan\frac{3}{(6c-9)^{\frac{1}{2}}}\right\} + \frac{(\alpha^2+\beta^2)^2(1+\mathrm{i})(2c-3)}{20\alpha^2 c^2\delta\mu} - \frac{2\mathrm{i}}{5\alpha\delta(2c-3)} = \tfrac{3}{2} - c. \tag{16}$$

Although c must still be solved numerically from this implicit dispersion relationship, it is, nevertheless, much simpler than solving (11) or the Orr–Sommerfeld equation numerically. Care, however, must be exercised about the large-$\alpha\delta$ limit. Since the boundary-layer equation was derived with a long-wave expansion, the large-$\alpha\delta$ limit is strictly valid for large δ and small α/κ. For intermediate values of $\alpha\delta$, we solve (11) numerically by carrying out a Taylor expansion of ϕ in y. Three-dimensional neutral curves for $\theta = \frac{1}{2}\pi$ are plotted in figure 1. We compare the computed results for the maximum-growing wavenumber α_m and growth rate of two-dimensional waves on water to Pierson & Whitaker's (1977) exact result from the full Orr–Sommerfeld equation in table 2. As evident, for $\delta \in (0, 16)$, which corresponds to $R \in (0, 700)$ for water, the error in α_m is no more than 6%. The error in the growth rate is more significant at low δ, at about 10%, but reduces rapidly to less than 2% for R in excess of 30. The results for large $\delta(\delta > 1.0)$ are in virtual agreement with the analytical estimate of (16). These results verify the validity of the boundary-layer equation for fluids in table 1 with small ϵ. As reviewed by Lin (1983), the linear prediction of α_m is in general agreement with experimental wave data in the inception region. The

boundary-layer theory hence offers an accurate description of the linear inception region even at high Reynolds numbers.

For nonlinear stationary waves propagating at a constant speed c, a Lagrangian transformation of (9) to the moving frame yields the equation for the stationary travelling waves on a vertical plane,

$$\frac{\partial}{\partial x}[u(u-c)]+\frac{\partial}{\partial y}(uv)=\frac{1}{5\delta}\left(h_{xxx}+\frac{1}{3}\frac{\partial^2 u}{\partial y^2}+1\right), \tag{17a}$$

$$\frac{\partial u}{\partial x}+\frac{\partial v}{\partial y}=0, \tag{17b}$$

$$\frac{\partial}{\partial x}\int_0^h (u-c)\,\mathrm{d}y=0, \tag{17c}$$

$$y=h(x): \quad \frac{\partial u}{\partial y}=0, \tag{17d}$$

$$y=0: \quad u=0, \quad v=0. \tag{17e,f}$$

We shall be interested in stationary waves with wavelength $l=2\pi/\alpha, (h,u,v)(x)=(h,u,v)(x+l)$. As the wavenumber α approaches zero, the waves become solitary waves. In constructing these waves, one could assume either that all waves correspond to the same flow rate

$$q=\frac{1}{l}\int_0^l\int_0^h u\,\mathrm{d}x\,\mathrm{d}y \tag{18}$$

or that all of them have the same average thickness h_{N}

$$\langle h\rangle=\frac{1}{l}\int_0^l h\,\mathrm{d}x=1. \tag{19}$$

If the constant-flux condition (18) is imposed, the average flux should be equal to the Nusselt velocity and q is unity identically. If the constant-thickness condition (19) is used, q is typically higher than unity. The two conditions yield similar but not identical results. The results are also mutually transformable with some effort. We choose to impose (19) since $\langle h\rangle$ cannot vary in time for periodic boundary conditions.

For near-critical conditions ($\delta\to 0$), the neutral wavenumber $\alpha_0=(18\delta)^{\frac{1}{2}}$ of (12b) vanishes, suggesting a weakly nonlinear, long-wave expansion. If we impose the relative order that the amplitude is of third order as the inverse wavelength, as Nepomnyaschy (1974), Lin (1974) and Demekhin *et al.* (1983) have done for the full equation, we obtain the KS equation for the limit of vanishing δ:

$$H_\tau+4HH_\xi+H_{\xi\xi}+H_{\xi\xi\xi\xi}=0, \tag{20}$$

where $H=\frac{3}{2}(h-1)/\alpha_0^3$, $\xi=(x-3t)\alpha_0$ and $\tau=\alpha_0^4 t$. Transforming (20) to a moving coordinate system with speed μ (a deviation speed) and integrating once, one obtains

$$H_{\xi\xi\xi}+H_\xi-\mu H+2H^2=Q, \tag{21}$$

where

$$Q=\langle 2H^2\rangle$$

is the deviation flux in the moving frame obtained by invoking the constant-thickness condition (19) and $\langle\ \rangle$ denotes averaging over one wavelength in the scaled ξ-coordinate. It is then clear that, for weakly nonlinear waves described by the KS

equation, waves tend to increase the liquid flux if the average thickness remains the same. This constant-thickness equation must be solved in conjunction with the deviation form of (19),

$$\langle H \rangle = 0. \tag{22}$$

If, however, the constant-flux condition is imposed, (21) reduces to

$$w_{\xi\xi\xi} + w_{\xi} - \lambda w + 2w^2 = 0 \tag{23}$$

and (22) is unnecessary and no longer holds, $\langle w \rangle \neq 0$. It is easy to relate the speeds and wave profiles of the two approaches by comparing (23) to (21):

$$\lambda = \pm(8Q + \mu^2)^{\frac{1}{2}} \tag{24a}$$

and

$$w = H - \tfrac{1}{4}\mu \pm (\tfrac{1}{16}\mu^2 + \tfrac{1}{2}Q)^{\frac{1}{2}}. \tag{24b}$$

The constant-flux equation has one less parameter and involves only one equation, whereas two equations, (21) and (22), must be solved for the constant-thickness approach and two parameters, Q and μ are involved. Consequently, the former is typically the preferred approach (Chang 1986) for analytical estimates of the stationary waves. For full numerical resolution of (17), however, these advantages are lost. In fact, the condition of zero mean deviation thickness of (22) allows us to remove the zeroth harmonic of our Fourier expansion of H. Hence, (22) is trivially satisfied and the numerical effort is reduced. Consequently, we choose the constant-thickness formulation here. Relationships between the two approaches, such as (24), are difficult to derive for the full equation, but for small deviation flow rates Q or small mean deviation thickness $\langle w \rangle$ (24) is still applicable.

There is yet a subtle difference between these two formulations in the KS limit of vanishing δ. Integrating (23) over a wavelength, one obtains $\lambda \langle w \rangle = 2\langle w^2 \rangle$. Since $\langle w^2 \rangle$ and $\langle w \rangle$ both cannot vanish, this implies that λ cannot be zero. Hence, all waves in the constant-flux formulation are travelling waves in the Lagrangian frame moving with speed 3. This is, however, not true for the constant-thickness formulation (21) and standing waves are then permitted, namely waves that propagate at exactly three times the average velocity in the laboratory frame are possible. We shall show in the next section that such standing waves do exist for (21) and they correspond to travelling waves of (23) studied in Chang (1986). It is also clear from the above argument that waves that travel faster (slower) than three times the average velocity have a larger (smaller) average film thickness than the waveless flat film in the constant-flux formulation. This conclusion would seem counterintuitive unless one remembers that the waves are not mass-carrying – they travel faster than the fluid elements. Many of the wave families of the full equation (17) can be traced from the stationary KS equation (21) or (23). Many of the wave selection mechanisms of the full system can also be deciphered by an analysis of the KS evolution equation (20) even when the analogy is not strictly correct. One valid analogy can be obtained by carrying out a bifurcation analysis of (23) for bifurcations of stationary solutions off the trivial solution $w = 0$ corresponding to the Nusselt flat film. Converting (23) to a dynamical system for $(w, w_{\xi}, w_{\xi\xi})$ as in Chang (1986) and analysing the three-dimensional Jacobian for the trivial solution, one concludes that at $\lambda = 0$ ($c = 3$), the spectrum of the Jacobian contains a purely imaginary pair of eigenvalues $\pm$i and a simple zero. The former corresponds to a Hopf bifurcation which yields a family of periodic stationary waves with a wavenumber that approaches unity at $\lambda = 0$. The Hopf bifurcation is supercritical with respect to $-c$ and hence the periodic stationary wave family, which bifurcates off the Nusselt flat film has a speed bounded above by $c = 3$ that decreases

with increasing amplitude and, as it turns out from the Hopf analysis, a wavenumber that also decreases with increasing amplitude. This is the origin of the slow γ_1 family. The unit wave number at $\lambda = 0$ corresponds to the neutral wavenumber $\alpha_0 = 1$ of the trivial basic state in (20). At larger δ, a slow γ_1 family of stationary periodic waves will continue to bifurcate supercritically from the Nusselt flat film with the neutral wavenumber α_0 and its wavenumber ranges continuously within the interval $(0, \alpha_0 \approx (18\delta)^{\frac{1}{2}})$. The amplitude of this wave family approaches zero as the wavenumber approaches α_0 and hence the waves near the neutral curve are the nearly sinusoidal ones characteristic of small-amplitude periodic solutions near a Hopf bifurcation point. The zero eigenvalue of the Jacobian for (23) at $\lambda = 0$ corresponds to a simple bifurcation that yields a new flat-film solution known as the 'conjugate' solution. As shown in the next section, the fast γ_2 family bifurcates off this conjugate solution. The Hopf simple bifurcation can be analysed with a high-order bifurcation theory (Chang 1986, 1989) which also yields information about the solitary wave limits of the two families. A detailed weakly nonlinear (bifurcation) analysis of how stationary periodic solutions bifurcate off the neutral curve can be found in the earlier work of Cheng & Chang (1990, 1992*a*, *b*). The technique is different from the classical Stuart–Landau formalism which carries out the expansion about the 'nose' of the neutral curve and is hence strictly valid for near-critical conditions. The neutral curve of the falling film does not have a parabolic 'nose' and thus requires a modified treatment.

3. Stationary waves of the Kuramoto–Sivashinsky equation and the origin of fast waves

We shall trace all stationary waves of the boundary-layer equation (17), in conjunction with the constant-thickness condition (19), as a function of δ and l. (The speed c is determined by the periodicity condition and is not a free parameter.) The experimentally observed waves will be shown to correspond to two wave families that trace their origins to the primary standing and travelling waves of the KS equation (21) at $\delta = 0$. The stationary waves of the KS equation (21) have been reported by Tsvelodub & Trifonov (1989), Kevrekides, Nicolaenko & Scovel (1990) and Demekhin, Tokarev & Shkadov (1991). However, we shall examine some unreported fine structures of the solutions that will be pertinent to the solutions of the boundary-layer equation at finite δ. We first observe the symmetry of the KS equations (21) and (23) with respect to the transformation

$$H \to -H, \quad \mu \to -\mu, \quad \xi \to -\xi, \tag{25a}$$

or

$$w \to -w, \quad \lambda \to -\lambda, \quad \xi \to -\xi. \tag{25b}$$

This property is sometimes known as reversibility and it implies that for every stationary wave that propagates in one direction, there is negative twin with an inverted and reflected profile ($w \to -w$ or $H \to -H$ and $\xi \to -\xi$) propagating with the same speed but in opposite direction ($\lambda \to -\lambda$ or $\mu \to -\mu$) relative to the critical speed of (12*a*). We shall distinguish the backward ones (negative solitary waves) from the forward ones (positive solitary waves) by a negative subscript (e.g. C_{-1} and C_1).

The reversible symmetry (25*b*) of the constant-flux formulation is especially intriguing. In Chang's (1989) analysis of a weakly nonlinear evolution equation of higher-order than (20) of the falling film and in other analyses of similar equations at different conditions (Chang 1986; Prokopiou *et al.* 1991), two families of waves were found with the constant flux-condition: γ_1 with a negative deviation speed $\lambda_1 < 0$ and

γ_2 with a positive speed $\lambda_2 > 0$. Moreover, the families are symmetric about $\lambda = 0$, namely $\lambda_1 = -\lambda_2$, for near-critical conditions. The origin of this symmetry can be seen in (23). This constant-flux condition actually allows two flat-film solutions: $w_1 = 0$ and $w_2 = \frac{1}{2}\lambda$. The former is simply the deviation form of the Nusselt flat film while w_2 is a unique 'conjugate' solution that arises because, in a Lagrangian frame, there is another flat-film solution that can sustain the same flow rate. Returning to (17), it is clear that the velocity profile for a flat film is $u = 3y(h - \frac{1}{2}y)$ and inserting this into the integral of (17), one obtains $h(c - h^2) = c - 1$. Hence, for c larger than $\frac{3}{4}$, which is always true, a conjugate flat-film solution exists in addition to $h = 1$,

$$h = \tfrac{1}{2}[-1 + (4c-3)^{\frac{1}{2}}] \sim 1 + \tfrac{1}{3}(c-3),$$

which is exactly $w_2 = \frac{1}{2}\lambda$ after the proper transformations. This additional flat-film solution whose thickness is dependent on the speed of the moving frame is also seen in the drag-out problem in coating flow (Tuck 1983). The existence of a conjugate solution is essential since shock-like stationary solutions, which are observed in falling films (Alekseenko, Nakoryakov & Pokusaev 1985) and other coating flows, require two flat-film solutions in the moving frame. Linearizing (20) about the conjugate solution, one finds that waves that appear on this conjugate flat film travel at a speed different by a factor -2λ from those on the Nusselt flat film. Hence, for every slow wave bifurcating from the Nusselt flat film with speed $-|\lambda|$, one expects a symmetric fast wave with speed $|\lambda|$ from the conjugate flat film. This is also seen in the reversibility condition (25*b*) for the KS equation. We recall that standing waves are not permissible in the constant-flux formulation. If one transforms the two travelling wave families, with symmetric speeds about $\lambda = 0$ or $c = 3$, of the constant-flux formulation to the constant-thickness formulation by (24), these two families collapse to a single standing wave family for α close to α_0. There is, however, a pitchfork bifurcation at smaller α which again gives rise to two travelling wave families with positive and negative μ (see figures 2 and 5). Hence, although the conjugate flat-film basic state does not exist for the constant thickness for obvious reasons, the two symmetric families of travelling waves that appear in this formulation can still be traced back to the existence of two flat-film basic states of the constant-flux formulation. The origin of the fast γ_2 wave family via a bifurcation off the conjugate flat-film solution is the preferred physical explanation. Both families persist at larger δ in both formulations.

In figure 2, we depict a more detailed version of the stationary wave solution branches reported in Demekhin *et al.* (1991). There is a myriad of infinite wave families. Owing to the symmetry of (21), a mirror image of figure 2 exists for μ negative. However, only a few families are pertinent to the boundary-layer equation. The primary branch S is a standing wave solution for (21) with $\mu = 0$. It hence represents a family of waves that travel at a constant speed equal to the critical speed $c_0 = 3$ of (12*a*). It is a travelling wave family for the constant-flux equation (23) with non-zero λ except at its bifurcation point $(\lambda, (\alpha/\alpha_0)) = (0, 1)$ where α is the wavenumber in the original x-coordinate and not the normalized ξ-coordinate of (20). A twin branch S_{-1} with speed $-\mu$ exists by virtue of (25). For both families, the wavenumber lies within the bound $(\alpha/\alpha_0) \in [1, 0.49775]$. At 0.49775, the S branch of (21) coalesces with a second branch $S^{(2)}$ which bifurcated from $(\alpha/\alpha_0) = \frac{1}{2}$. The $S^{(2)}$ branch is identical to S except that two waves are contained in one wavelength which is twice as long as the corresponding one on S. Likewise, $S^{(n)}$ branches bifurcate from $(\alpha/\alpha_0) = 1/n$ and they are all identical to S except that n units exist in one wavelength. We first focus on S. All along the S branch, the waves are nearly sinusoidal with longer waves having a larger second-harmonic content and hence a steeper front edge (see figure 3). These

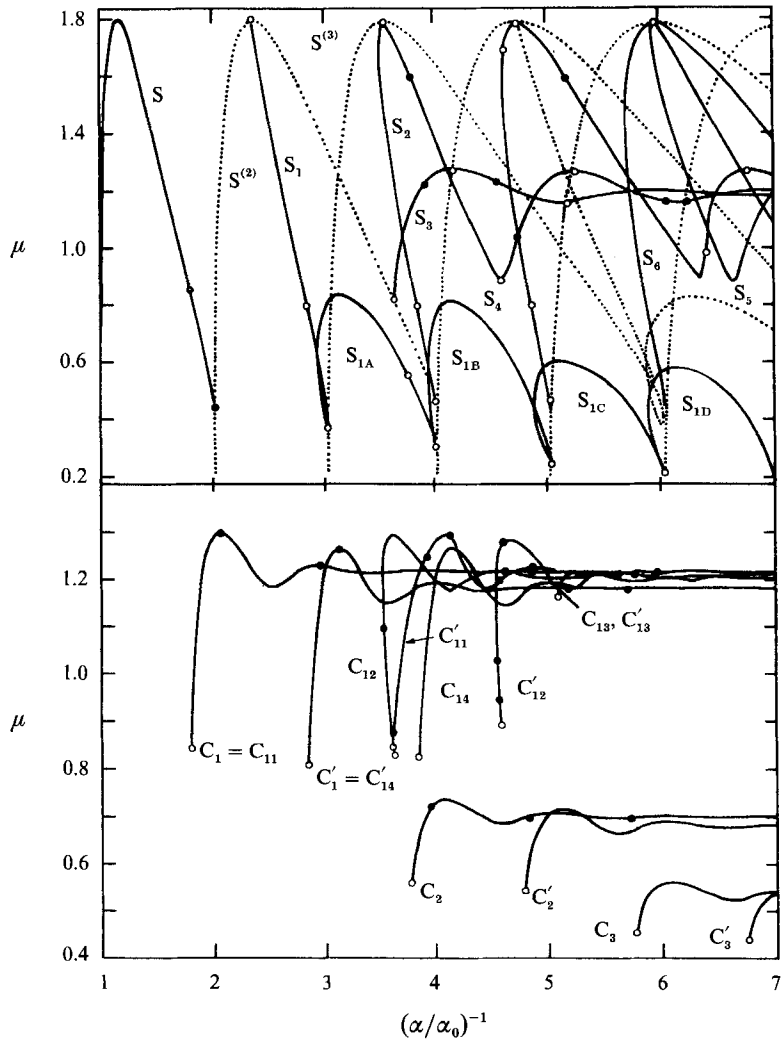

FIGURE 2. Stationary solution branches of the Kuramoto–Sivashinsky equation. The C_n families bifurcate from the circles at the top half of the diagram. New solutions (tori) bifurcate from C_n at the marked points.

waves are the ones near the neutral curve and they are the ones amenable to the Stuart–Landau normal mode expansion formalism suggested by Benney (1966) and subsequently carried out by Gjevik (1970), Lin (1974), Nakaya (1975) and Chang (1989). However, as pointed out by Chang (1989), waves longer than twice $2\pi/\alpha_0$ contain many Fourier modes that cannot be easily resolved with a normal mode expansion. These waves are contained in two families of secondary branches. One family consist of the S_n branches that come off the $S^{(n)}$ branches. As is evident in figure 3, at the bifurcation point on $S^{(n)}$, the waves on S_n are still quite sinusoidal but subsequent ones develop very rich structure with a broad Fourier content. Some of them (S_2, S_3, S_5, S_6, etc.) extend to $\alpha = 0$ and terminate at solitary waves. Unlike the $S^{(n)}$ branches, these branches do not resemble each other. A subset of the S_n family are the branches S_{1A}, S_{1B}, etc. that were not reported by Demekhin *et al.* (1991). A second family of waves consists of C_n and C'_n branches in figure 2. In contrast to the $S^{(n)}$ and

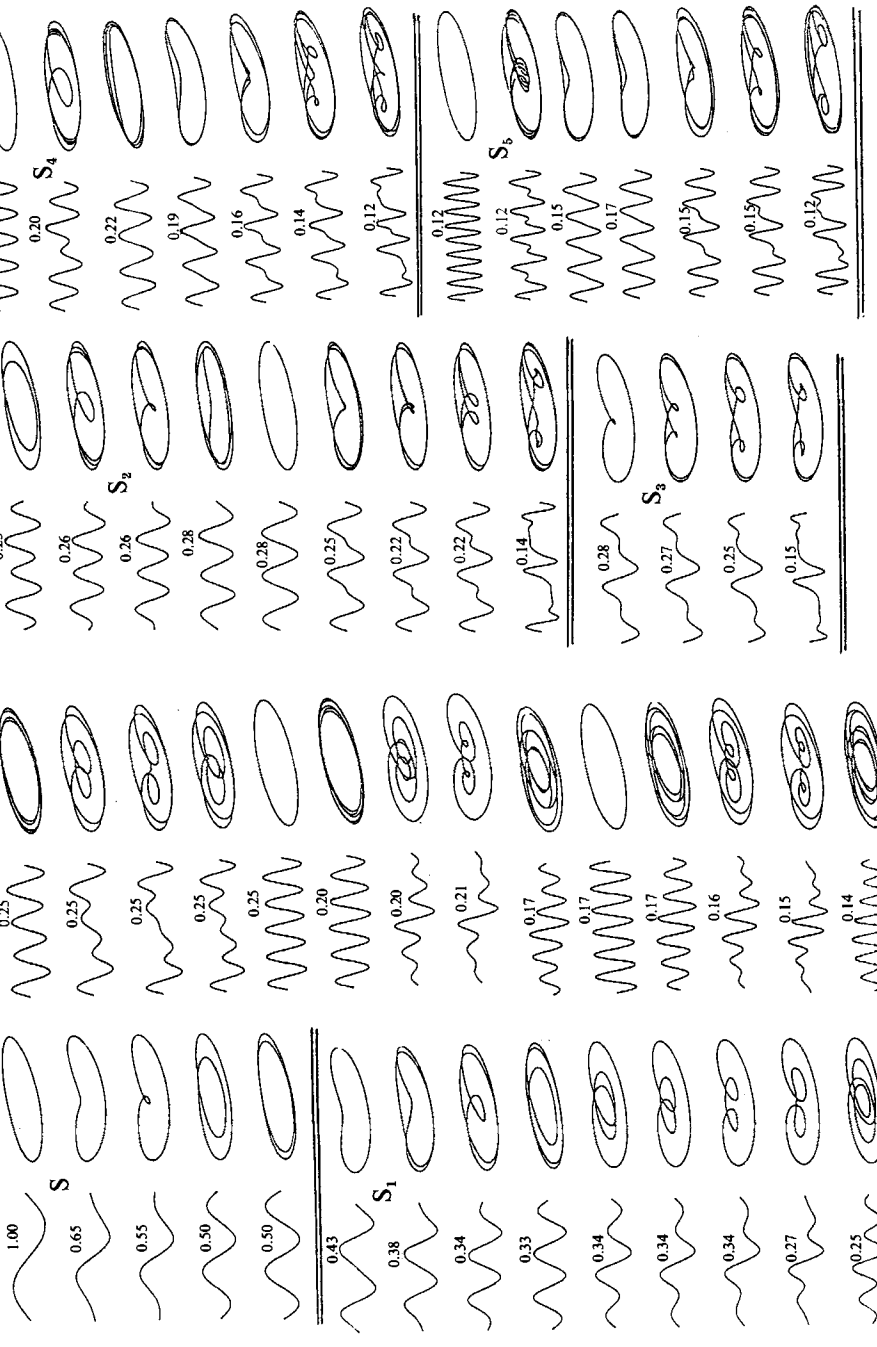

FIGURE 3. Wave profiles $H(\xi)$ of the KS equation for the constant-thickness formulation and their corresponding closed trajectories in the phase space of (H, H', H''). The numbers are the normalized wavenumber (α/α_0).

S_n families, these are travelling wave solutions of (21) with c in excess of 3. As shown in figure 4, these travelling waves have unique solitary wave shapes that we have classified in a different report (Chang, Demekhin & Kopelevich 1993). The primary one is C_{11}, which will also be called C_1, bifurcates off S at $(\alpha/\alpha_0) = 0.5547$. This forwarding propagating branch is the only important branch in the C_n family that will survive at finite δ. In contrast, all inverted ones C_{-n} participate in the pertinent wave branches at finite δ. This C_1 branch has been studied by Tsvelodub (1980) and Armbruster, Guckenheimer & Holmes (1988) and, in their formulation, it corresponds to a travelling wave which is annihilated at a homoclinic bifurcation. The homoclinic bifurcation corresponds to an infinitely long solitary wave here as the C_1 branch extends to vanishing α in figure 2. As evident in figure 3, both the S_n and C_n families and their inverted twins with negative μ consist of waves with a large band of Fourier modes. Chang (1986, 1989) suggested that these waves can be described by elliptic functions provided by an analysis in the solitary ($\alpha \to 0$) limit. For the constant-flux formulation, the homoclinic orbit corresponding to the solitary wave can be approximated by a heteroclinic cycle joining the fixed point corresponding to the Nusselt flat film $w_1 = 0$ to the conjugate flat film $w_2 = \frac{1}{2}\lambda$. Hence, an estimate of the amplitude of the solitary wave is simply $w_{\max} = \frac{1}{2}\lambda$. However, by multiplying (23) by w and integrating from $\xi = -\infty$ to $+\infty$, one obtains

$$\int_{-\infty}^{\infty} w^2(2w-\lambda)\,\mathrm{d}\xi = 0,$$

which stipulates that $w_{\max} > \frac{1}{2}\lambda$, and the above estimate must be considered as a tight lower bound of the amplitude of a solitary wave in the constant-flux formulation. In the solitary wave limit, the deviation flux $Q = \langle 2H^2 \rangle$ approaches zero for the constant-thickness formulation in the limit of vanishing amplitude. Consequently, (24) suggests that all solitary waves of the constant-thickness formulation of the KS equation can also be approximated by the amplitude–speed correlation $H_{\max} = \frac{1}{2}\mu$ as μ and $H_{\max}$ approach zero. This is confirmed to within our numerical accuracy in the solitary wave limits of the C_n branches in figure 4, which also shows that $H_{\max} = \frac{1}{2}\mu$ is a lower bound on amplitude, albeit a tight lower bound. This, of course, also ensures agreement with the C_{-n} families by the symmetry argument. The only branches of importance at finite δ are S, C_1, C_{-n} and the S_{1A}, S_{1B}, S_{1C} series. With finite δ, the reversibility symmetry is broken and waves are not exactly symmetric about $\mu = \lambda = 0$ or $c = 3$. However, the S family and the C_{-1} family coalesce to form the slow γ_1 family with a negative solitary wave limit, and C_1 and S interact to form a fast γ_2 family with a positive solitary wave limit (see figure 5). Since the S family of standing waves correspond to travelling waves in the constant-flux formulation, this division into γ_1 and γ_2 travelling wave families was already in place at $\delta = 0$ for that formulation. At larger δ, interactions with the other standing and travelling wave branches lead to hybrid branches of γ_2. Otherwise, the division of wave families into the slow and fast γ_1 and γ_2 families remains intact. These two families of stationary waves share a common feature: their amplitude increases with their wavelength such that the solitary wave limit of each family is the largest wave. In fact, owing to symmetry (25), while the solitary wave limit of γ_2 (depicted as C_1 in figure 4) resembles the observed solitary wave, the solitary wave limit of γ_1 is an inverted version of C_1 (negative solitary wave) and is not observed experimentally. Because the wave amplitude is small only for short waves on γ_1 near the neutral wavenumber α_0, the weakly nonlinear Stuart–Landau formalism and the weakly nonlinear evolution equations like the KS equation are strictly applicable for these short waves on γ_1. They are typically invalid for the γ_2 family of fast waves except

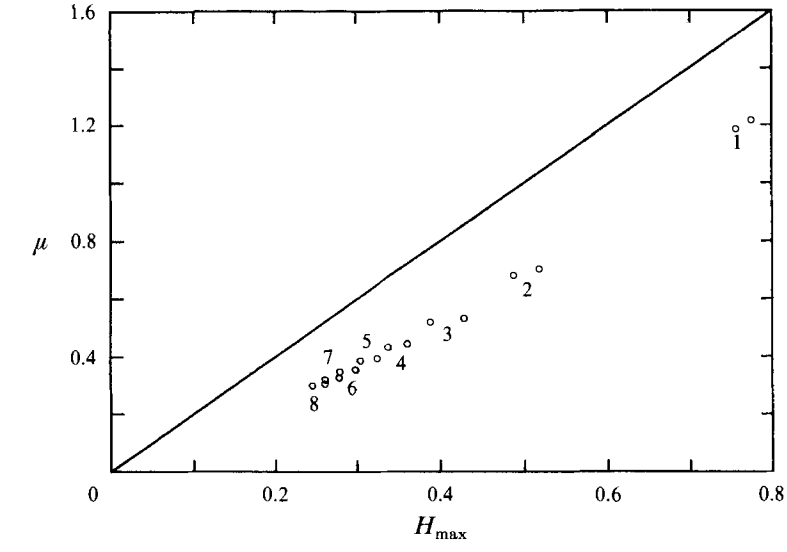

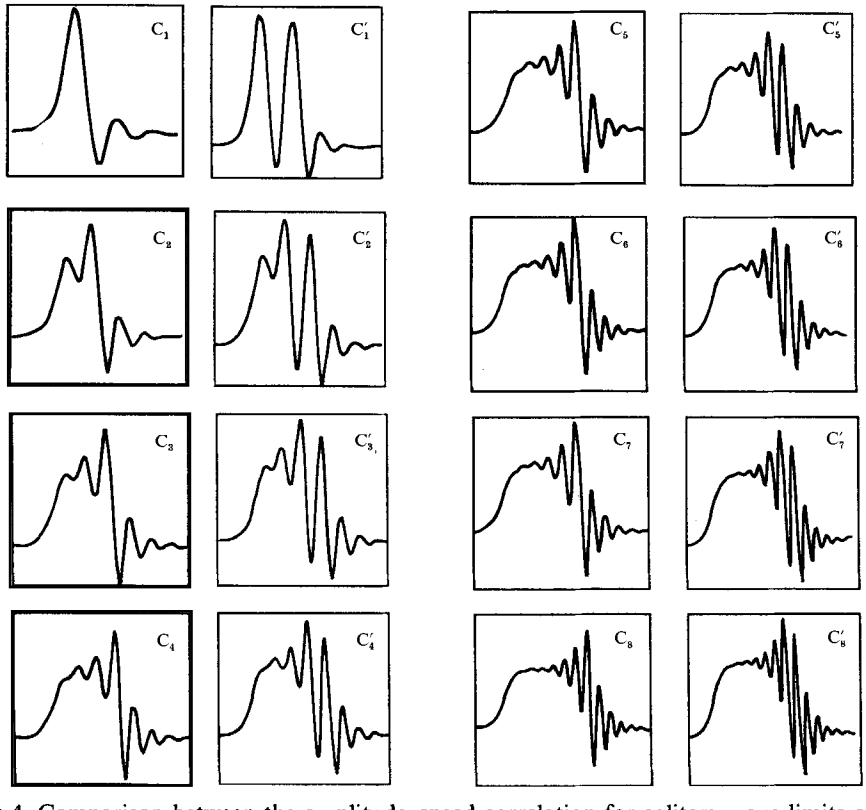

FIGURE 4. Comparison between the amplitude–speed correlation for solitary wave limits of the C_n branches and Chang's analytical estimate. The higher C_n and C_{-n} solitary waves are to the right of figure 2.

for near critical conditions when the wave amplitude on both families is small. Even then, the classical Stuart–Landau formalism must be replaced by high-order bifurcation theories (Chang 1989).

4. Stationary waves of the boundary-layer equation

Unlike the limiting case of vanishing δ for the KS equation, solution of the boundary-layer equation is considerably more difficult because of the need to resolve the flow field under the film and to track the free surface $h(x)$. Bach & Villadsen (1984) have used a Lagrangian finite-element formulation to track the free surface and less than three elements in y to resolve the flow field. However, a Lagrangian formulation requires a rezoning procedure to untangle the convoluted meshes and is hence difficult to implement at high Reynolds number on δ when more y-elements are required. Kheshgi & Scriven (1987) and Ho & Patera (1990) use a different approach, where the Lagrangian formulation is applied only in the y-direction to allow accurate front tracing without mesh entanglement. We shall use the same mixed Lagrangian–Euler method here. However, because the third-derivative curvature term h_{xxx} that appears in our boundary-layer equation is numerically undesirable, we do not apply a direct finite-element decomposition. Instead, we divide the film into N layers in the y-direction and by manipulating the projected equations, eliminate the h_{xxx} term from all but one equation. The decomposition in the x-direction is a spectral Fourier expansion. The result of this mixed Euler–Lagrangian and spectral-element formulation is that the exponential convergence (with respect to mode number) of the spectral method is combined with the numerical advantages of the finite-element method such as the elimination of the undesirable h_{xxx} term, higher-order bases that mimic the averaged equation formulation and a narrowbanded projected differential operator, all of which facilitate the iteration step. With this formulation, this difficult free-surface problem requires about three to seven layers to achieve convergence. This implies only a factor of 10 increase in the number of equations compared to the KS equation. However, even with these simplifications, a systematic construction of all stationary waves and a detailed stability analysis of these waves remain numerically impossible for the full equations of motion. This is why the boundary-layer approximation is invoked here. If the full Navier–Stokes equation is used, the strong nonlinearities in h at the interface and the flow field will render the solution considerably more difficult, especially during the Newton iteration step. Because of the numerous tricks involved in our numerical formulation, we sketch in Appendix B our numerical treatment of the boundary-layer equations in (17).

We note that the numerical formulation in Appendix B with quadratic polynomial expansion at every element reduces to the averaged equation if only one element is used ($N = 1$). This is one reason for using the simple expansion at every layer. Straightforward calculation shows that in this leading-order approximation

$$h^3h''' + \delta[6(q-c)^2 - c^2h^2]h' + [h^3 - q - c(h-1)] = 0 \tag{26}$$

is obtained. This equation must be solved in conjunction with the constant-thickness condition (19). Stationary waves of this averaged equation have been studied by Shkadov (1967, 1968), Bunov, Demekhin & Shkadov (1984), Demekhin & Shkadov (1985) and Trifonov & Tsvelodub (1985, 1991). All our stationary wave branches obtained in the full equation (17) are in quantitative and qualitative agreement with the stationary wave solutions of (34) for $\delta < 0.06$. Beyond this value, considerable difference is seen. The unique bifurcation sequence of γ_2 in figure 5 is notably missing

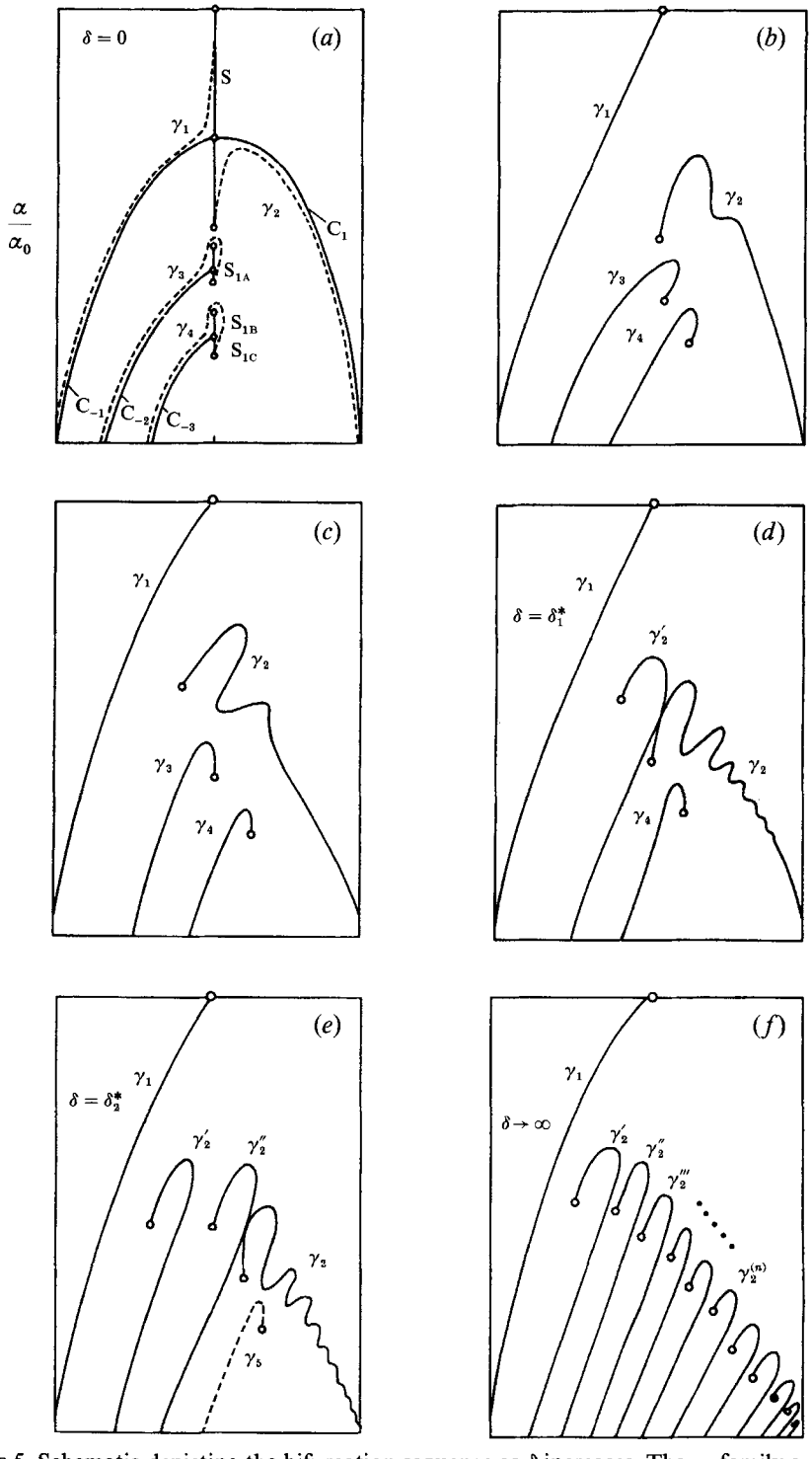

FIGURE 5. Schematic depicting the bifurcation sequence as δ increases. The γ_1 family survives intact. It consists of short, near-sinusoidal waves for $(\alpha/\alpha_0) \to 1$ and a one-hollow inverted solitary wave for $(\alpha/\alpha_0) \to 0$. The $\gamma_2^{(n)}$ families, born by successive coalescence of the γ_2 branch with γ_n in a pinching bifurcation, are detached from the neutral wavenumber $(\alpha/\alpha_0) = 1$ and do not possess near-sinusoidal waves. The γ_2 branch ends as a one-hump positive solitary wave while $\gamma_2^{(n)}$ ends as an $(n+1)$ hollow negative solitary wave. However, the $\gamma_2^{(n)}$ waves away from the solitary wave limit resemble positive solitary waves (see figure 7).

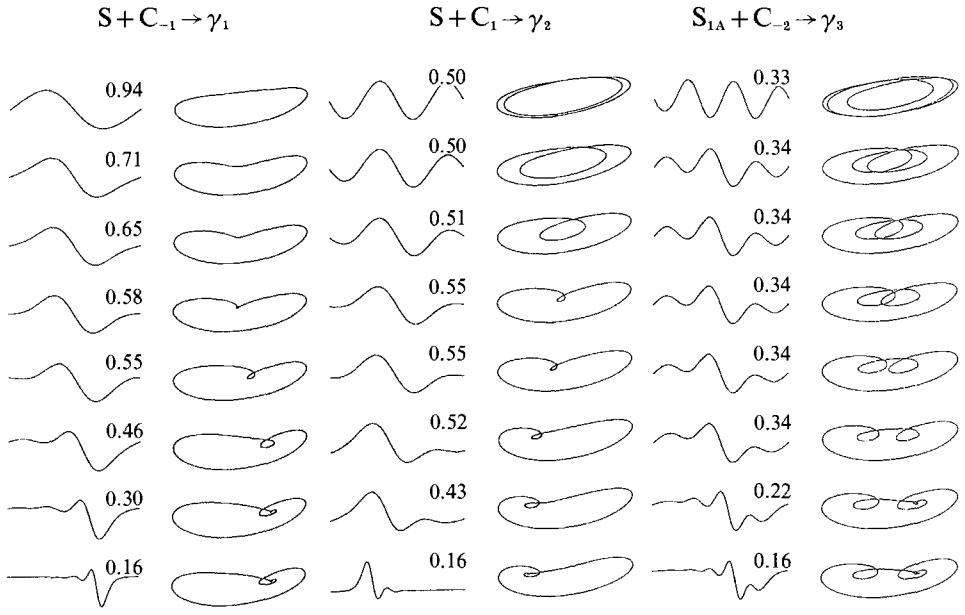

FIGURE 6. The imperfect bifurcations that occur at $\delta = 0^+$ which coalesce several branches of the KS equation to form the new γ_n branches. Only the γ_2 branch approaches a one-hump positive solitary wave limit as (α/α_0) approaches zero. The γ_1 family ends as a one-hollow negative solitary wave and the γ_n families ($n \geqslant 3$) culminate in an $n-2$ hollow negative solitary wave.

from the averaged equation. This then implies that the averaging is strictly valid for low Reynolds numbers, $R < 10$ for water, as evident from table 1.

We first sketch the changes in the solution structure qualitatively. If plotted on the c–α parameter space, the stationary wave solutions of the KS equation (21) in figures 2 and 3 collapse into a very simple structure. All the $S^{(n)}$ families can now be represented by the primary S branch which spans $(\alpha/\alpha_0) \in (1, 0.49775)$ along the $c = 3$ line in figure 5(*a*). The S_n branches appear at lower wavenumbers but they do not participate in the creation of important branches at finite δ and hence are omitted in figure 5. The remaining standing waves S_{1A}, S_{1B}, S_{1C} etc. are also marked in figure 5. They are drawn disjoint to show that the subsequent bifurcations will separate them. We note that since these branches bifurcate subcritically with respect to α^{-1} before turning around, each point on the indicated segments may represent two waves. The primary travelling waves C_1 and C_{-1} that bifurcate from S and its inverted counterpart are also shown in figure 5 as a pitchfork bifurcation with speeds in excess of and less than 3, respectively. For a non-zero δ, the pitchfork undergoes an imperfect bifurcation such that two travelling wave branches, γ_1 and γ_2, are born as shown in figure 5(*a*). Likewise the C_{-n} branches coalesce with the S_1 branches to form $\gamma_3, \gamma_4, \gamma_5$ etc. for $\delta \neq 0$. The C_n branches also give rise to new solutions but they will not participate in the future evolution of the solution branches. The only pertinent branches will be shown to be γ_n for $\delta \neq 0$. From the wave profiles in figure 6, it is clear that only γ_2 terminates at $\alpha = 0$ with a positive solitary wave. The remaining branches all culminate in an inverted solitary wave with a hollow instead of a hump. The branch γ_2 is clearly faster than the critical linear speed $c_0 = 3$ while the other branches are either slower or close to 3. This relative speed with respect to 3 will change as δ increases but γ_2 remains the fastest branch. It should also be pointed out that $\gamma_3, \gamma_4, \gamma_5$, etc. retain the topologies of C_{-2}, C_{-3}, C_{-4} etc. and exhibit in the solitary wave limit two hollows, three hollows,

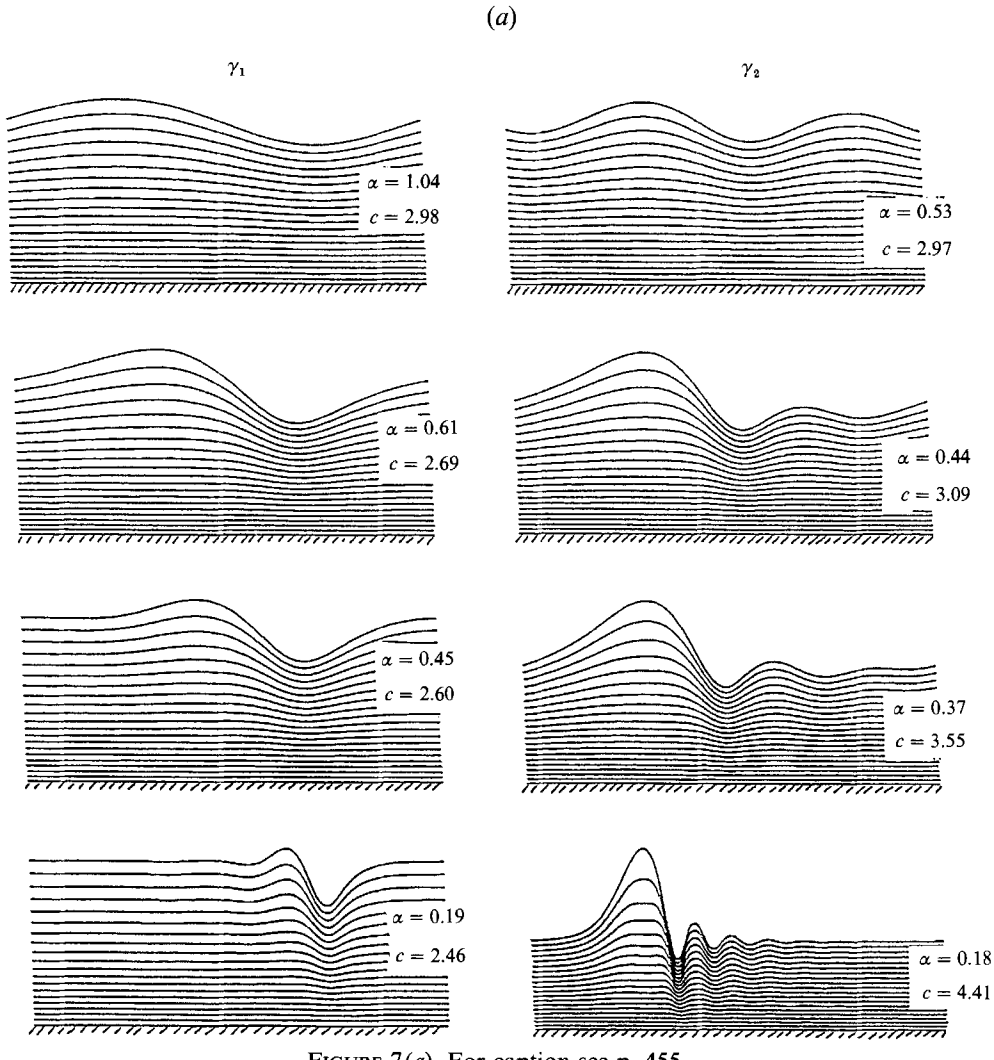

FIGURE 7(*a*). For caption see p. 455.

etc. (Chang *et al.* 1993). The actual profiles of these branches at low δ are shown in figure 6.

The above bifurcation features for small δ are consistent with those exhibited by the averaged equation (26). However, for $\delta > 0.06$, the γ_2 branch begins to wrinkle as γ_3 and γ_4 move towards it. This and all subsequent evolution is distinct from the averaged equation. We also note that for $\delta > 0.06$, the velocity profile of the waves definitely deviates from the parabolic profile assumed in the averaged equation. At $\delta_1^* \approx 0.09$, the turning point of γ_3, originating from the imperfect bifurcation at $\delta = 0$, coalesces with a turning point of γ_2 to yield an isolated branch γ_2' in a unique 'pinching' isola point. As shown in figure 5, this pinching occurs successively as δ increases as γ_2 coalesces with γ_4, γ_5, etc. to yield γ_2'', γ_2''', respectively. The γ_2'' branch is born at $\delta \approx 0.15$ as shown in the wave profiles of figure 7. The $\gamma_2^{(n)}$ branches resemble their mother branches $C_{-(n+1)}$ of the KS equation with $(n+1)$ hollows in the solitary wave limit (see figure 4). However, prior to the solitary wave limit, they can take on shapes that resemble a positive solitary wave with one big hump as the small hollows resemble capillary bow

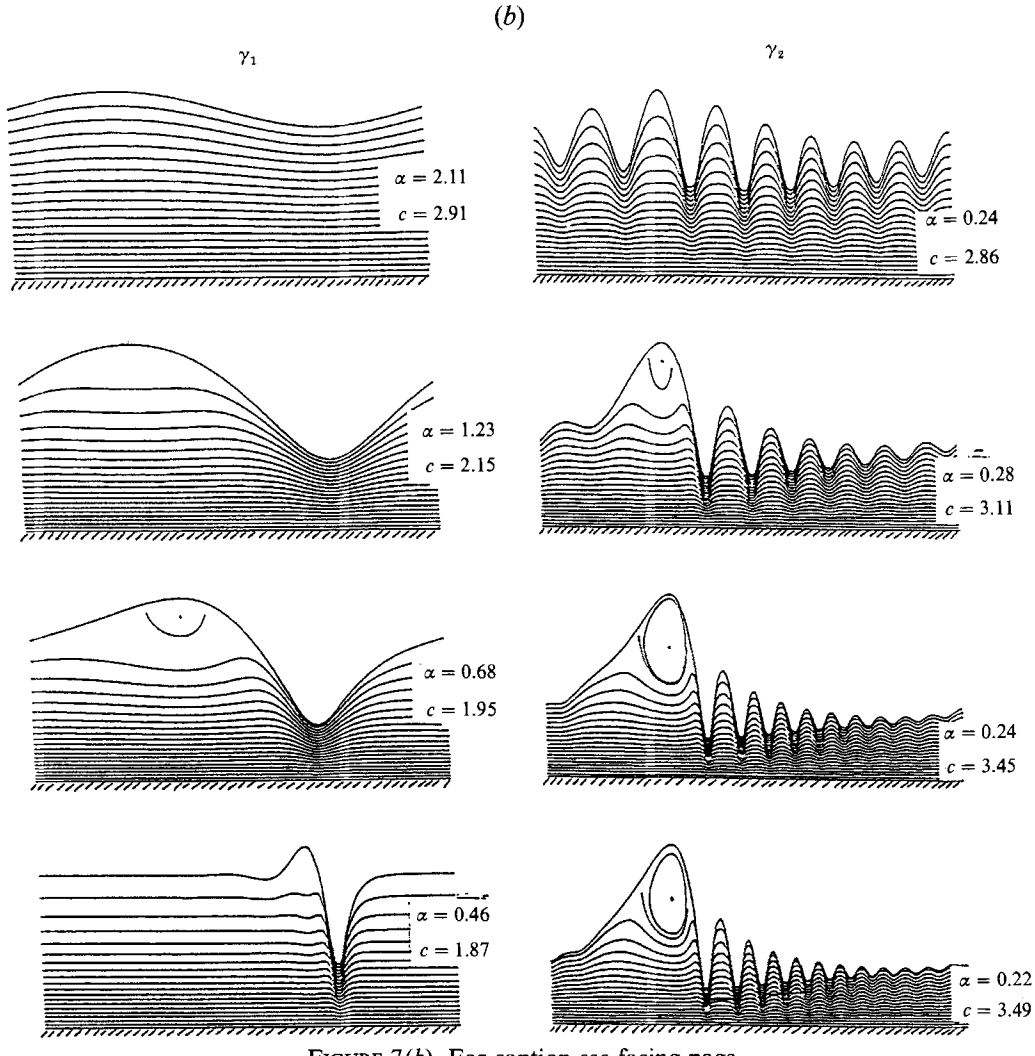

FIGURE 7(*b*). For caption see facing page.

waves. In the limit of infinite δ, the original γ_2 branch has given rise to an infinite family of these $\gamma_2^{(n)}$ branches. In figure 8, the actual computed solution branches are shown. It is seen that the symmetry about $c = 3$ of the KS equation is broken. The γ_2 family increases in amplitude and speed as δ increases much more than the γ_1 family. This is also evident in figure 7 which shows the positive near-solitary waves of γ_2 are much larger and much faster in absolute deviation speed from 3 than their negative solitary wave counterparts on γ_1.

We note that the periodic waves in figure 6 correspond to closed trajectories in the phase space of (h, h_x, h_{xx}). In the solitary wave limit ($\alpha \to 0$), these limit cycles approach a fixed point corresponding to the Nusselt flat film $(h, h_x, h_{xx}) = (1, 0, 0)$. They hence approach a homoclinic orbit connected to the fixed point whose eigenspectrum contains one real eigenvalue and a pair of complex conjugates. All stationary wave branches in our study at finite δ approach homoclinicity and hence have a solitary wave limit. An intriguing property of dynamical systems that possess homoclinic orbits linked to a hyperbolic fixed point with a real and a complex

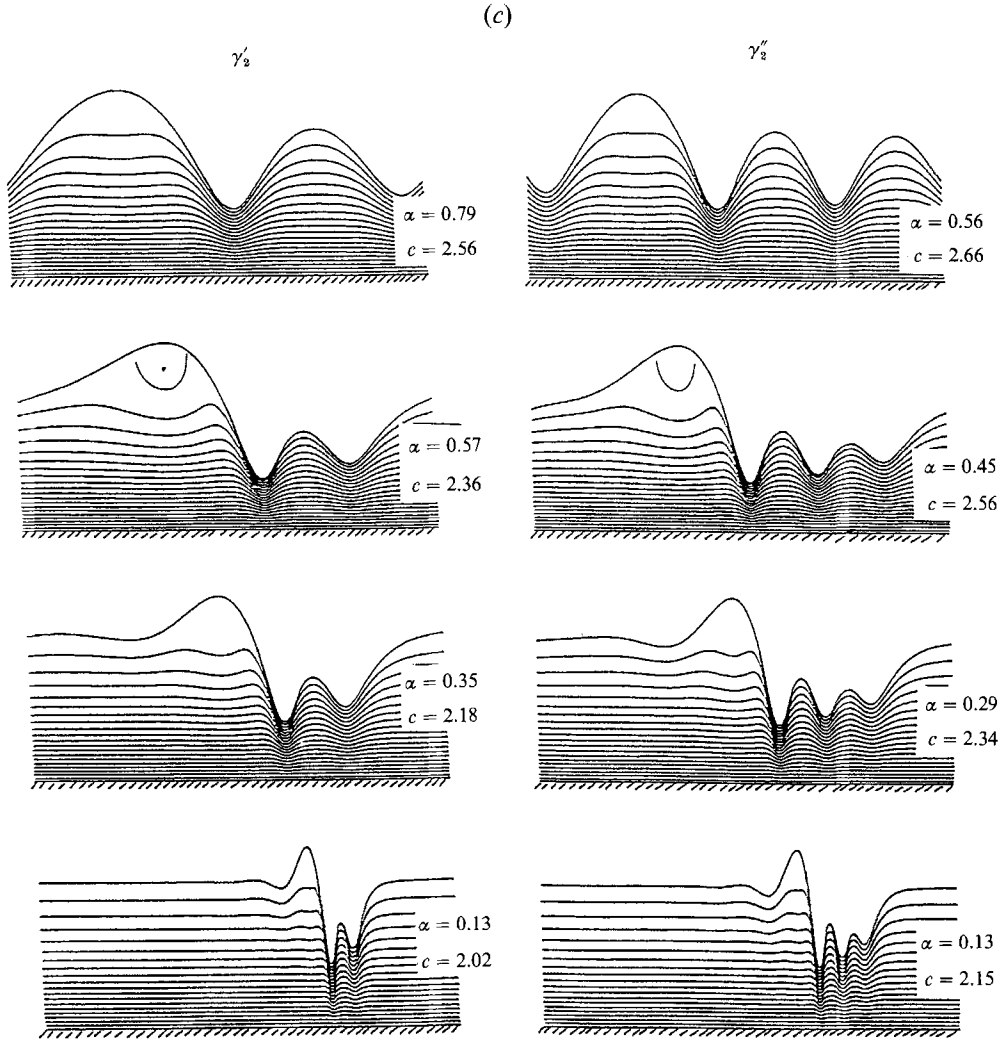

FIGURE 7. Wave profiles and streamlines below the interface of waves on γ_1 and $\gamma_2^{(n)}$ for (*a*) $\delta = 0.062$ and (*b*, *c*) 0.27.

conjugate pair of eigenvalues is that bifurcations near homoclinicity can be qualitatively discerned with information on the eigenspectrum of the fixed point only. We can then use the elegant theorem of Sil'nikov to explain the pronounced wrinkling of the γ_2 branch (and the weaker wrinkling of the γ_1 branch) in figure 8. Each wrinkle corresponds to a saddle node bifurcation of the limit-cycle solution branch as it approaches homoclinicity. (See Chang *et al.* 1993 for a more detailed discussion on a related problem.) In all cases studied here, the flat-film fixed point corresponding to the KS equation in (21) or (23) or the averaged equation (26) for $c > 3$ all yield one real eigenvalue σ_1 and one complex conjugate pair with a real part σ_2. The signs on σ_1 and σ_2 are different and are dependent on whether the positive or solitary waves are involved. The eigenvalues are responsible for the wiggling near the fixed point in the phase space and the capillary bow waves of the real wave profile, and the real eigenvalue for the gentle slope on the other side of the solitary waves. One also reaches the same conclusion regarding the spectrum of the 'fixed point' corresponding to the

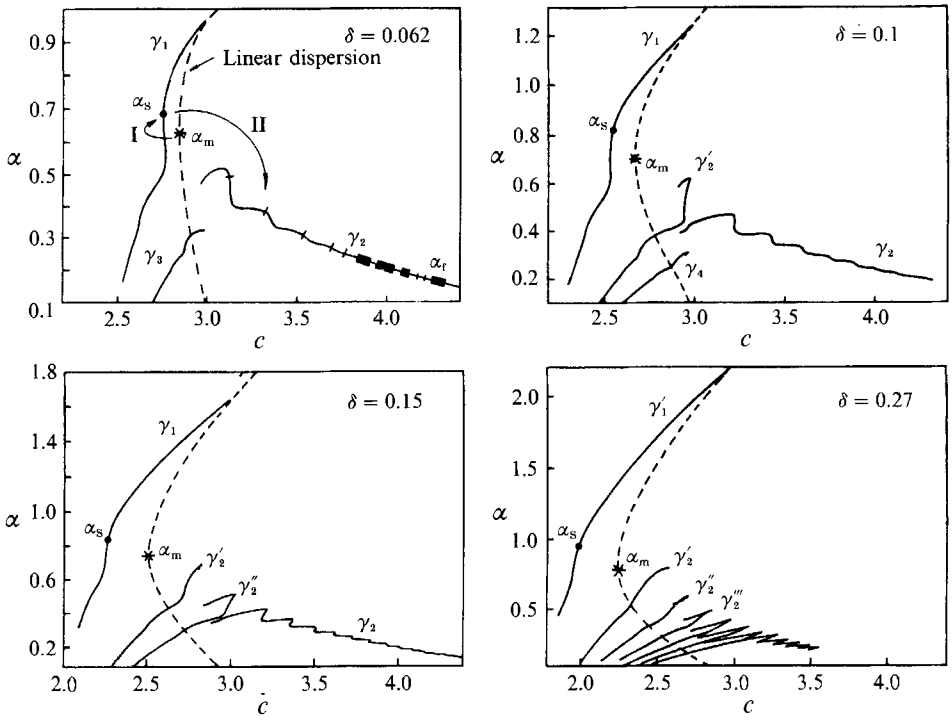

FIGURE 8. Actual computed wave branches for $\delta = 0.062$, 0.1, 0.15 and 0.27 and comparison to the linear dispersion curve. The fastest growing linear wave α_m and the most stable waves on the wave branches are represented by stars, circles and blackened segments in some figures. The wave transitions are indicated in the first figure.

full boundary-layer equation (17) at $x \to \pm\infty$. According to Sil'nikov's theorem (proven in more detail by Glendinning & Sparrow 1984), if $|\sigma_2/\sigma_1|$ is less than unity, one expects a periodic orbit to undergo an infinite sequence of saddle node bifurcations with increasing period as it approaches the homoclinic orbit in the parameter space. The distance between two adjacent saddle nodes also decreases monotonically as the periodic solution branch winds towards homoclinicity. Since a periodic orbit corresponds to a periodic wave here, the saddle node bifurcations of the periodic solution branch are exactly the wrinkles seen on γ_1 and γ_2 as the solitary wave limit is approached. We have found $|\sigma_2/\sigma_1|$ to be less than unity in all of our calculations and the wrinkles are hence expected.

Several comparisons to earlier nonlinear analyses can be made here. We first note that, at large δ, the solitary wave of the slowest branch γ_1, approaches a speed of about $1.5\,\langle u\rangle$ which is close to the $1.67\,\langle u\rangle$ predicted by Prokopiou *et al.* (1991) using the averaged equation. This shows that the averaged equation may be reasonably accurate in the estimate of the wave speed of the slowest solitary wave on the γ_1 branch even though the local velocity profile beneath the hump and the bow waves is far from parabolic for δ in excess of 0.06. The averaged equation fails to describe γ_2 and its hybrid families $\gamma_2^{(n)}$ completely. The wave profiles of some of the branches are shown in figure 7. We note that, for δ in excess of say 0.1, the only near-sinusoidal waves appear on γ_1. Even the shortest waves on the $\gamma_2^{(n)}$ families are much longer than the near-sinusoidal ones on γ_1 and they possess wave profiles with large Fourier contents. This implies that for moderate δ and beyond, the observed near-sinusoidal waves just beyond the inception region must all lie on the slower γ_1 branch while the solitary

waves that evolve downstream lie on the faster γ_2 and $\gamma_2^{(n)}$ branches. This scenario will be confirmed in the next section and it explains the initial deceleration of waves out of the inception region and the subsequent acceleration as they evolve from the near-sinusoidal regime into the solitary wave region observed by Stainthorp & Allen (1965).

In comparing our results to experimental wave profiles, we shall sometimes select a wave of the same wavelength $l = 2\pi/\alpha$ as the measured one for a given δ and compare the wave speeds c and wave profiles $h(x)$. In some cases, only the wave period, $T = l/c$, is given on a strip chart and we shall then compare the wave period instead of c. If the wave speed c is measured accurately, we shall locate a wave of the same speed and compare l or T and $h(x)$. Finally, the Reynolds number $\langle R \rangle$ of most reported data is based on the true flow rates for films with waves, which is not identical to our R based on the flat film h_N. An iteration is then necessary to compute q of (18) and relate the two Reynolds numbers. For a given wave profile with wavelength l measured at a specific $\langle R \rangle$, we begin by assuming $\langle R \rangle = R$ and obtain δ and α by the following formulae:

$$h_N = (3\nu^2/g)^{\frac{1}{3}} R^{\frac{1}{3}}, \quad \langle u \rangle = (\tfrac{1}{3} g\nu)^{\frac{1}{3}} R^{\frac{2}{3}},$$

$$\delta = 3^{-\frac{7}{9}} 5^{-1} \gamma^{-\frac{1}{3}} R^{\frac{11}{9}}, \quad \kappa = 3^{-\frac{2}{9}} \gamma^{\frac{1}{3}} R^{-\frac{2}{9}}, \quad \alpha = 2\pi\kappa h_N / l.$$

After completing the numerical calculation for the given δ and α, we obtain an improved estimate of R by setting

$$R = \langle R \rangle / q.$$

Typically, three iterations suffice to yield an accurate estimate of R.

In figure 9, we compare our computed wave tracings to the experimental ones of Nakoryakov *et al.* (1985) of the same period T at various $\langle R \rangle$. The computed values of δ, α and c are shown in table 3 along with the wave family that the wave profile belongs to. In some cases, two waves on different families, γ_2 and γ_2', have the same wavelength as the measured one. It is clear that the wave on γ_2 is always the selected one. All waves were measured in the solitary regime and all of them appear on the positive one-hump branch γ_2 or on segments of the γ_2' branch which resemble a one or two hump solitary wave. (The γ_2' family eventually evolves towards a negative solitary wave with two hollows as evident in figure 9.) In figure 10, we compare our results to the only water wave tracing, offered by Stainthorp & Allen (1965). It was taken at 5 cm below the distributor and corresponds to the spatial station at the beginning of the acceleration stage from near-sinusoidal waves to solitary waves. Since the speed of the profile was reported at $c = 0.22$ m/s at $\langle R \rangle = 15$, we shall locate waves of the same speed. Two waves, one on γ_1 and the other on γ_2', are found to have this wave speed. The one on γ_1 is slightly longer with $l = 1.10$ cm and the one on γ_2' is 1.03 cm long. Both are in satisfactory agreement with the value of 1.0 ± 0.2 cm estimated from the wave tracing (figure 9 of their paper). However, on closer examination of the detailed wave shapes, it is clear that the γ_2' wave is selected. This again confirms that the acceleration beginning at 5 cm from the distributor signals the departure from the nearly sinusoidal γ_1 family and the approach towards waves on the $\gamma_2^{(n)}$ families. Finally, in figure 11, we offer comparison to the classical photographs of Kapitza (1948) and Kapitza & Kapitza (1949). The parameters are listed in table 4. Good agreement is again evident. Whenever there is a choice between a wave on the γ_2 family and one on γ_2', the γ_2 wave is always the chosen one. The somewhat lower amplitude of the photographed waves can be due to distortion by the tube curvature during the imaging.

The above favourable comparison to measured profiles verifies the boundary-layer approximation. The only remaining task is then to decipher why specific waves on

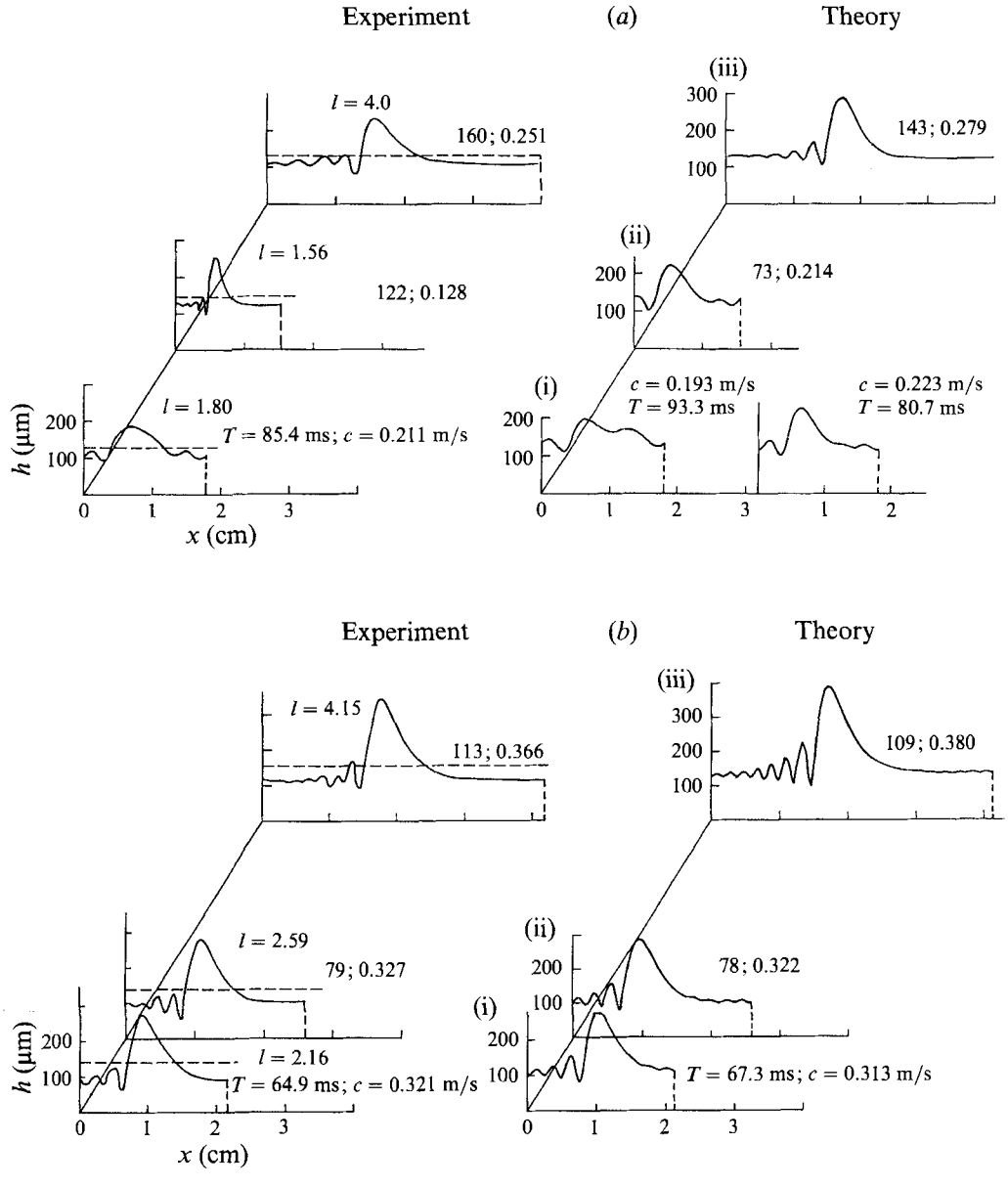

FIGURE 9(*a*, *b*). For caption see facing page.

certain branches are selected. We expect this selection mechanism to be related to the relative stability of the waves with respect to two-dimensional and three-dimensional disturbances of all wavelengths. The latter disturbance should also be more dominant on the $\gamma_2^{(n)}$ families since the two-dimensional solitary waves break up into three-dimensional non-stationary waves downstream. We shall confirm these speculations with a stability analysis in the next section.

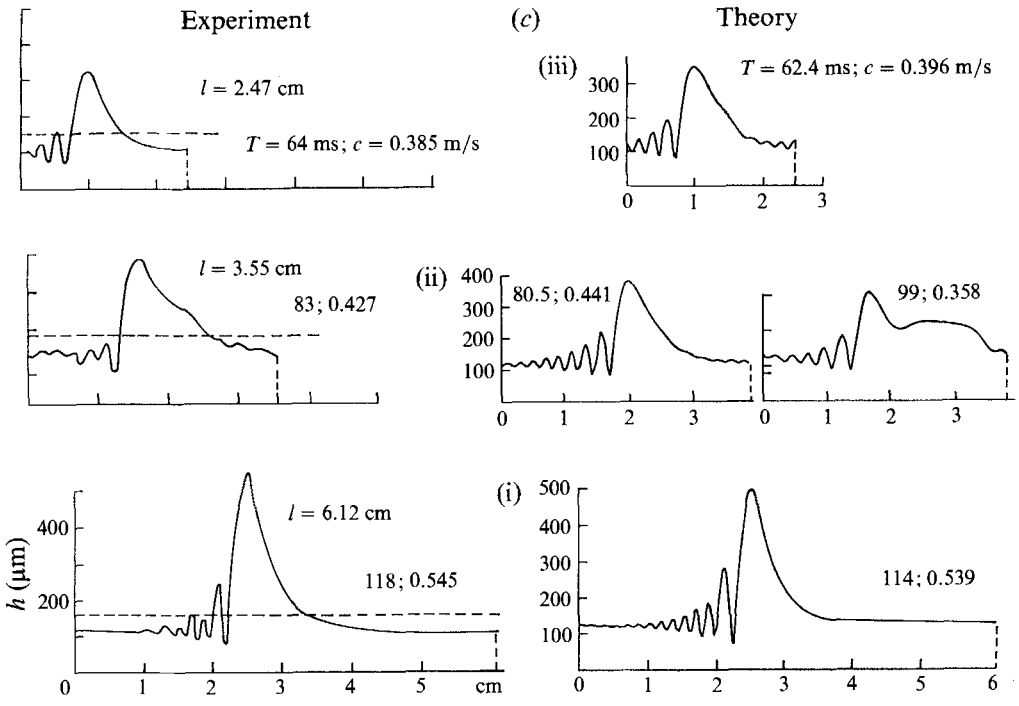

FIGURE 9. Comparison to the wave data of Nakoryakov *et al.* (1985) for the same wave period. The wave period and speeds in ms and m/s are indicated. The wave parameters are listed in table 3. All are near solitary waves on γ_2 and γ_2'. (*a*) $\langle R\rangle = 10$, (*b*) 18.8, (*c*) 31.

(*a*) $\langle R\rangle = 10$ (water)

	δ	α	c	Wave family
(i)	0.09205	0.3673	2.8015	γ_2'
	0.08208	0.3661	3.4412	γ_2
(ii)	0.08273	0.4299	3.2877	γ_2
(iii)	0.07476	0.1628	4.5233	γ_2

(*b*) $\langle R\rangle = 18.8$ (water)

	δ	α	c	Wave family
(i)	0.1484	0.3210	3.5026	γ_2
(ii)	0.1448	0.2663	3.7606	γ_2
(iii)	0.1380	0.1650	4.4211	γ_2

(*c*) $\langle R\rangle = 31$ (water)

	δ	α	c	Wave family
(i)	0.2301	0.1218	4.7418	γ_2
(ii)	0.2465	0.2041	3.7389	γ_2
	0.3122	0.2085	2.6643	γ_2'
(iii)	0.2567	0.2942	3.2867	γ_2

TABLE 3. Wave parameters for figure 9

5. Stability and selection of stationary waves

One expects the waves exiting the inception region to be monochromatic waves with the fastest growing wavenumber α_m. However, slowly evolving finite-amplitude effects then stipulate that a subset of the stationary waves we constructed be selected successively downstream. Since the first stationary waves are short, near-sinusoidal ones and the only wave family with short-wave members is the slow family γ_1 (see figure

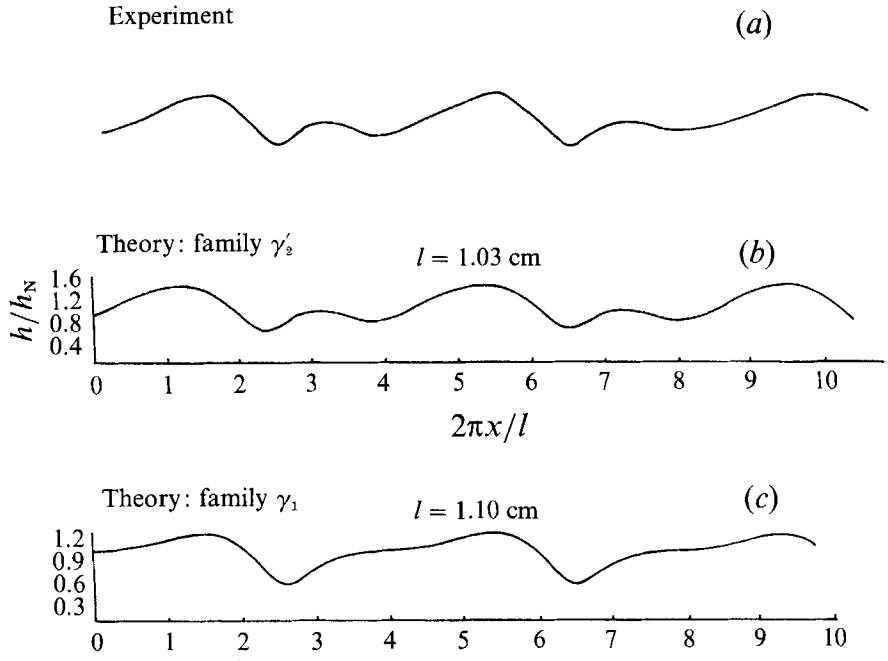

FIGURE 10. Comparison to the tracing of Stainthorp & Allen of the same speed measured at the boundary between the near-sinusoidal and the solitary wave regimes. The height is normalized by h_N and the length by $l/2\pi$.

8), we expect a short member of γ_1 to be selected first. This would then imply a deceleration of the wave speed immediately beyond inception which is consistent with the observation of Stainthorp & Allen. Further downstream, near solitary waves resembling the solitary waves on γ_2 and not those on γ_1 are observed. We hence expect the waves to evolve towards the solitary end of the fast family γ_2. This is again consistent with Stainthorp & Allen's observation of acceleration towards the solitary wave regime. We shall confirm and quantify these observations here by subjecting the stationary waves to three-dimensional disturbances of all wavelengths.

That the most stable or least unstable waves are selected in a particular wave family has been speculated since the first paper of Kapitza (1948). He suggested that a wave with the minimum average energy dissipation,

$$\dot{E} = -\left\langle \int_0^h \left[\left(\frac{\partial u}{\partial y}\right)^2 + \left(\frac{\partial v}{\partial x}\right)^2 \right] \mathrm{d}y \right\rangle, \tag{27a}$$

where $\langle\ \rangle$ denotes averaging over a wavelength, is the observed one. This argument originates from an inertialless energy stability analysis of (9) and one expects it to be valid only at low δ (or R) since inertia is surely also important at higher δ. However, this dissipation criterion will be shown to be quite accurate at low δ and it offers a very physical selection criterion in this limit. At low δ, α_0 is small and if one imposes the same small-amplitude, long-wave expansion carried out for the KS equation, it can be shown that

$$\partial u/\partial y \sim -3(y-h)$$

such that

$$\dot{E} \sim -3\langle h^3 \rangle$$

$$\sim -3 - 4\alpha_0^6 \langle H^2 \rangle. \tag{27b}$$

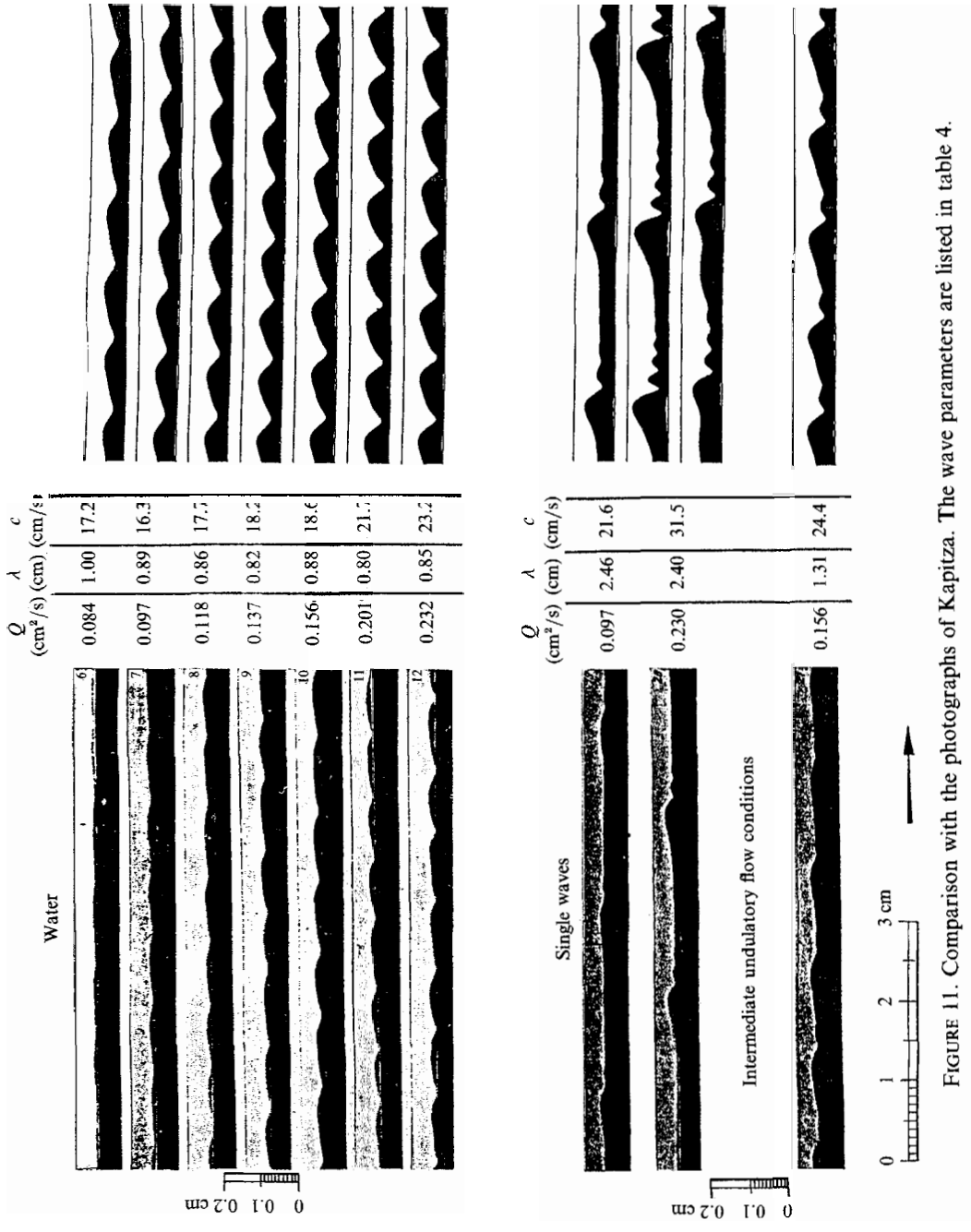

FIGURE 11. Comparison with the photographs of Kapitza. The wave parameters are listed in table 4.

Plates	Q (cm^2/s)	$\langle R\rangle$	l (cm)	R	q	δ	α	Exp. c (cm/s)	Theory c (cm/s)	Family
6	0.084	7.368	1	6.850	1.076	0.0627	0.639	17.2	15.4	γ_1
7	0.097	7.748	0.89	8.543	1.103	0.0725	0.728	16.3	16.3	γ_1
8	0.118	10.361	0.86	9.196	1.127	0.0898	0.767	17.7	17.7	γ_1
9	0.137	12.020	0.82	10.488	1.146	0.1055	0.817	18.2	18.8	γ_1
10	0.156	13.684	0.88	11.903	1.150	0.1232	0.772	18.6	19.6	γ_1
11	0.201	17.629	0.80	14.949	1.179	0.1628	0.871	21.7	21.9	γ_1
12	0.232	20.350	0.85	17.288	1.177	0.1944	0.833	23.2	23.0	γ_1
19	0.097	8.521	2.46	7.348	1.1597	0.0682	0.262	21.6	2.1	γ_2
20*a*	0.230	20.178	2.40	14.748	1.368	0.1600	0.290	31.5	33.2	γ_2
20*b*	0.230	20.173	2.40	17.159	1.176	0.1926	0.295	31.5	28.4	γ_2'
21	0.156	13.684	1.31	11.642	1.175	0.1199	0.517	24.4	22.7	γ_2

TABLE 4. Kapitza's data for water in figure 11

Since $\langle H^2\rangle$ corresponds to the deviation flux for a constant-thickness formulation, (27*b*) implies that at small amplitude and δ, the stationary wave selected among waves of the same average thickness is one with the highest flow rate. Shkadov (1968) also arrived at the above conclusion by subjecting the γ_1 family of the averaged equation to an elaborate two-dimensional sideband stability analysis. However, owing to the limitation of the averaged equation, he concluded that these waves with the maximum flow rates are stable to two-dimensional disturbances. We shall show that, for $\delta < 0.037$, Kapitza's dissipation criterion (27*a*) offers an excellent estimate of the least unstable wave on γ_1 which is, nevertheless, unstable to two-dimensional disturbances. The conclusion that the wave with the highest dissipation rate also carries the highest flux in criterion (27*b*) was derived with a small-amplitude expansion and is expected to be valid only for small-amplitude waves like the short members of the γ_1 family. Since the γ_2 family begins with large-amplitude waves, (27*b*) is not expected to hold for this fast family but the full criterion (27*a*) will be shown to remain as a good estimate. Cheng & Chang (1992*a*) have subjected the γ_1 family of the KS equation (with the constant-flux formulation) to two-dimensional and three-dimensional sideband disturbances and concluded that a band of short waves next to the neutral curve α_0 are unstable to two-dimensional disturbances while the ones close to the maximum-growing mode α_m are unstable to three-dimensional disturbances. There is a window of waves stable to all disturbances in between. The first result corrects the conclusion of the first attempt on finite-amplitude two-dimensional sideband instability by Lin (1974). The results by Nepomnyaschy (1974) for the S family of the KS equation suggest that even the long waves on γ_1 are unstable to two-dimensional sideband instability such that a narrow window of waves stable to sideband disturbances exists. However, in the solitary wave limit, one expects the stability of the finite-amplitude waves to be identical to that of a flat-film, namely unstable to all two-dimensional disturbances with wavenumbers within $(0, \alpha_0)$. Prokopiou *et al.* (1991) subjected the γ_1 waves of the averaged equation to subharmonic instability and found that a band of waves close to the neutral curve are also unstable to two-dimensional subharmonic disturbances. These analytical results then suggest that γ_1 waves close to the neutral curve are unstable to either two-dimensional subharmonic or sideband disturbances. Near solitary waves are unstable to the same two-dimensional disturbances of the flat film. The intermediate waves are more susceptible to three-dimensional disturbances.

If there is any window of stable waves, it should exist only if these instability regions do not overlap in the intermediate region near α_m. From the result of Cheng & Chang (1992*a*), for the KS equation, this stable window should exist only for vanishingly small δ. Demekhin & Kaplan (1989) confirmed this numerically and showed that at the KS limit of $\delta = 0$, the stable band is within $(\alpha/\alpha_0) \in (0.77, 0.84)$ which was first suggested by Nepomnyaschy (1974). Beyond $\delta = 0.037$, our numerical result below indicates that this stable window no longer exists. The entire γ_1 family is hence unstable. Nevertheless, one expects the existence of a least unstable member of the γ_1 family in the intermediate α range and it should be most susceptible to three-dimensional disturbances from the earlier results. There have been no prior stability study of the γ_2 family of fast waves.

Linearizing (10) about the stationary solution (u, v, h) of (17) and introducing the disturbance vector $(\hat{u}(x,y), \hat{v}(x,y), \hat{w}(x,y), \hat{h}(x)) \exp(\mathrm{i}\alpha\nu x + \mathrm{i}\beta z + \alpha\mu t)$ where the hat variables have the same wavelength as the stationary waves and are hence $l = 2\pi/\alpha$-periodic in x, ν is a real number between $(-\frac{1}{2}, \frac{1}{2})$ to span all nth subharmonics of α, β is the transverse wavenumber and $\alpha\mu$ is the complex growth rate, one obtains

$$\alpha\mu\hat{u} + \frac{\partial}{\partial x}(2u-c)\,\hat{u} + \mathrm{i}\alpha\nu\hat{u}(2u-c) + \frac{\partial}{\partial y}(u\hat{v} + v\hat{u}) + \mathrm{i}\beta u\hat{w}$$

$$= \frac{1}{5\delta}\left[\left(\frac{\mathrm{d}}{\mathrm{d}x} + \mathrm{i}\alpha\nu\right)^3 \hat{h} - \beta^2(\hat{h}_x + \mathrm{i}\alpha\nu\hat{h}) + \frac{1}{3}\frac{\partial^2\hat{u}}{\partial y^2}\right], \quad (28a)$$

$$\alpha\mu\hat{w} + \frac{\partial}{\partial x}(u-c)\,\hat{w} + \mathrm{i}\alpha\nu\hat{w}(u-c) + \frac{\partial}{\partial y}(v\hat{w})$$

$$= \frac{1}{5\delta}\left[\mathrm{i}\beta(\hat{h}_{xx} + 2\mathrm{i}\alpha\nu\hat{h}_x - \alpha^2\nu^2\hat{h}) - \mathrm{i}\beta^3\hat{h} + \frac{1}{3}\frac{\partial^2\hat{w}}{\partial y^2}\right], \quad (28b)$$

$$y = h: \quad \frac{\partial\hat{u}}{\partial y} = -\frac{\partial^2 u}{\partial y^2}\hat{h}, \quad \frac{\partial\hat{w}}{\partial y} = 0, \quad (28c)$$

$$y = 0: \quad \hat{u} = \hat{w} = 0, \quad (28d)$$

$$\alpha\mu\hat{h} + \frac{\partial}{\partial x}\left[\int_0^h \hat{u}\,\mathrm{d}y + u\hat{h}\right] + \mathrm{i}\alpha\nu\left[\int_0^h \hat{u}\,\mathrm{d}y + u\hat{h}\right] + \mathrm{i}\beta\int_0^h \hat{w}\,\mathrm{d}y = 0, \quad (28e)$$

$$\hat{v} = -\int_0^y \left(\frac{\partial\hat{u}}{\partial x} + \frac{\partial\hat{w}}{\partial y} + \mathrm{i}\alpha\nu\hat{u}\right)\mathrm{d}y. \quad (28f)$$

We note that the introduced disturbances correspond to constant-thickness perturbations. It is not clear whether the stability of the waves to such disturbances is the same as their stability to constant-flux disturbances. In Poiseuille flow, for example, there are subtle differences in the stability with respect to these two disturbances. The stability of the stationary solution (u, v, h) is then determined by the growth rate $\alpha\mu_R$ where μ_R is the real part of μ. Since the transformation $\nu \to -\nu$ simply yields the conjugate equation, we can restrict the bound of ν to $(0, \frac{1}{2})$. We decompose $h(x)$ into several layers as in Appendix B and carry out a Legendre expansion of the deviation variables within each layer. Taking inner products with the Legendre polynomials in a Galerkin-element formulation then yields the projected equation in the y-direction.

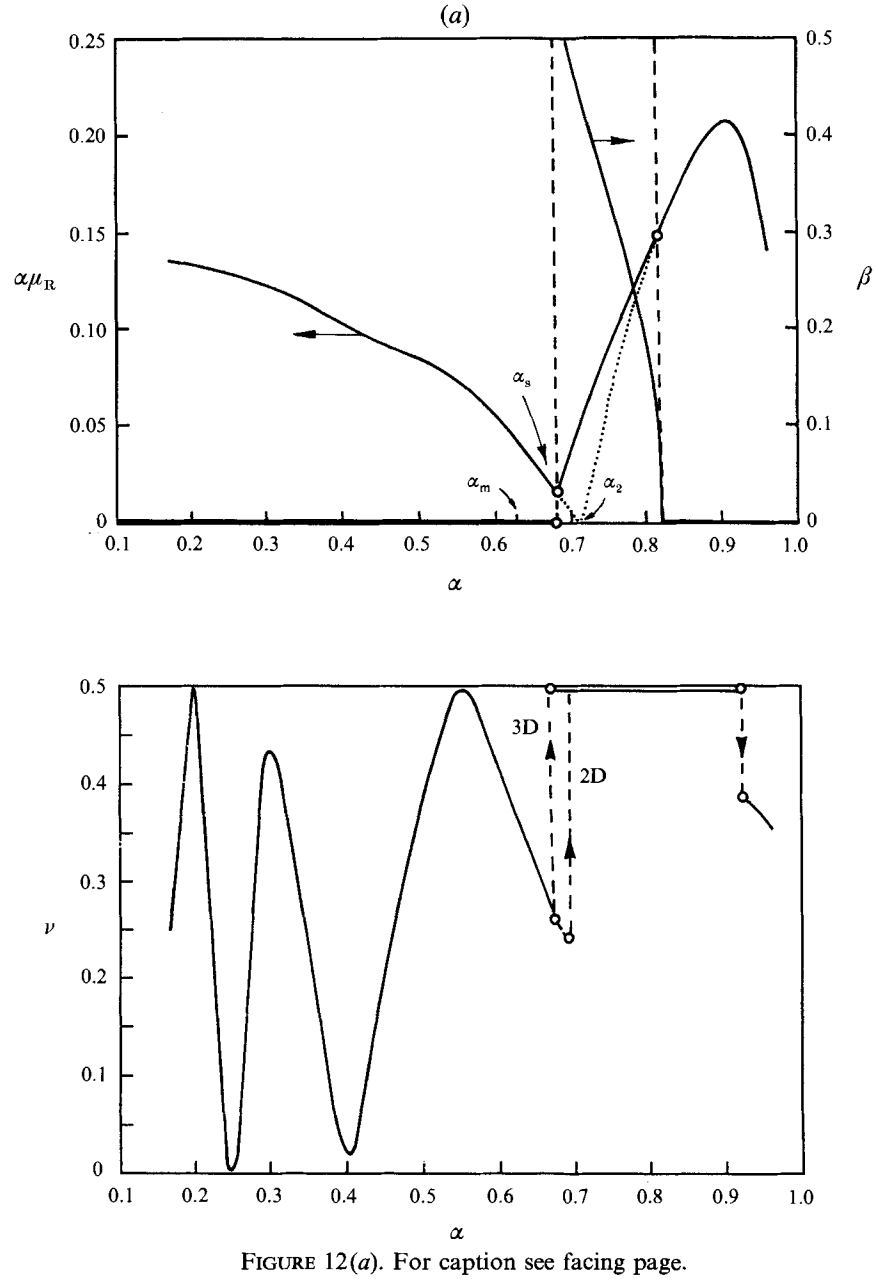

FIGURE 12(*a*). For caption see facing page.

Both zeroth and first derivatives are guaranteed to be continuous at the layer boundaries as before. Fourier expansion is then carried out in the x-direction. The end result is a generalized eigenvalue problem for complex matrices at a given α

$$|\boldsymbol{A}-\alpha\mu\boldsymbol{E}| = 0 \tag{29}$$

which is solved by means of a QR algorithm.

Typical computed growth rates of the dominant disturbances of the γ_1 family are

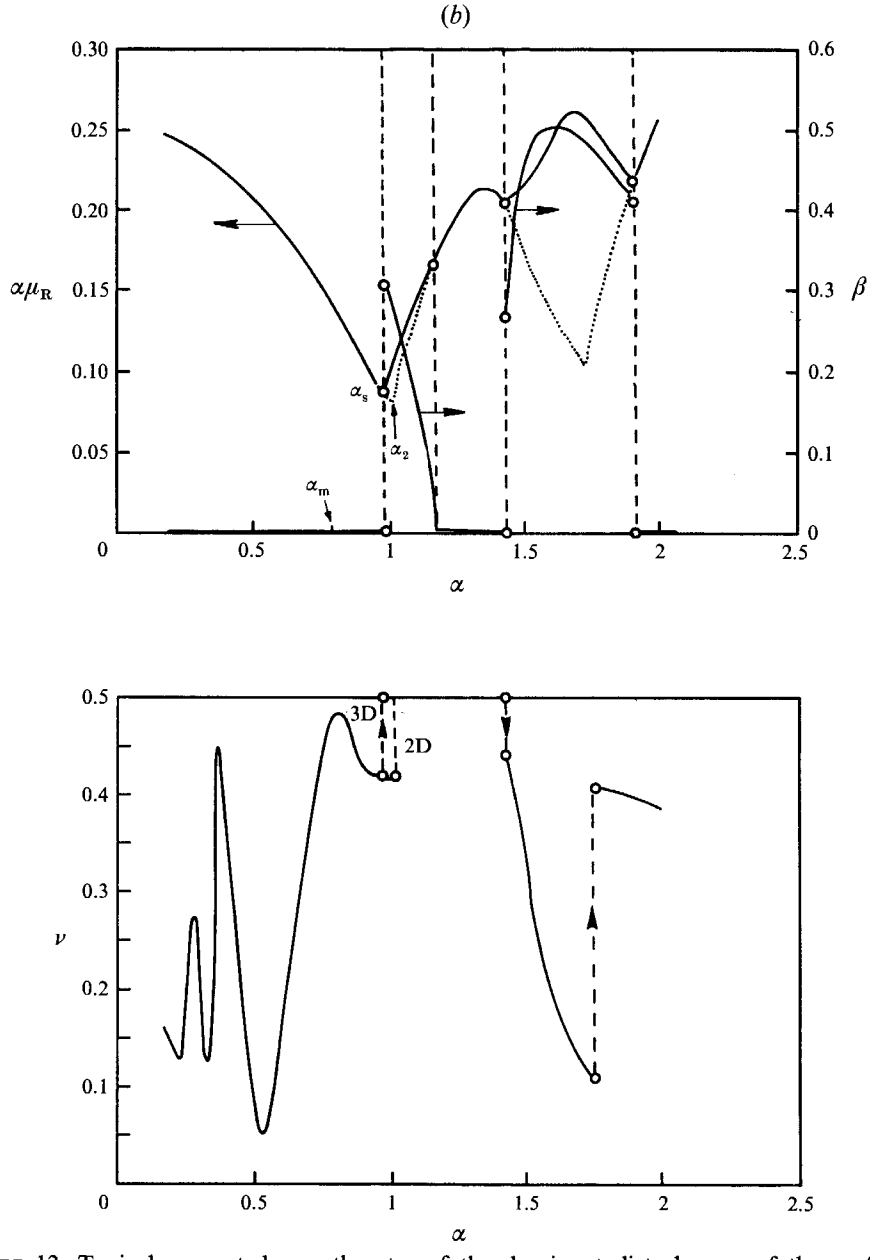

FIGURE 12. Typical computed growth rates of the dominant disturbances of the γ_1 family for $\delta = 0.062$ ($\alpha_2 = 0.711$, $\alpha_s = 0.675$, $\alpha_m = 0.623$) and $\delta = 0.27$ ($\alpha_2 = 1.006$, $\alpha_s = 0.975$, $\alpha_m = 0.78$). Three-dimensional disturbances are only dominant in the indicated windows within some of which α_2 and α_s lie. The depicted ν corresponds to these three-dimensional disturbances. The growth rates of the two-dimensional disturbances in these windows are only slightly lower and they are depicted by broken curves. (*a*) $\delta = 0.062$, (*b*) 0.27.

shown in figure 12 and table 5 for $\delta > 0.037$. Only the most unstable disturbance for every stationary wave is depicted. Many of the earlier predictions are confirmed. The short waves near the neutral curve are either unstable to two-dimensional sideband disturbances (ν small) or two-dimensional subharmonic disturbances ($\nu = 0.5$). The

2-dimensional disturbances

$\langle R\rangle_{H_2O}$	l (cm)	c (cm/s)	$2\pi/\nu\alpha$ (cm)	$\alpha\mu_R/\alpha c$	δ	α_2
7.36	0.897	15.38	7.89	0.0106	0.062	0.711
11.45	0.822	18.48	3.24	0.0993	0.10	0.811
16.47	0.778	21.38	2.29	0.198	0.15	0.889
21.13	0.751	23.69	1.94	0.267	0.20	0.945
27.22	0.726	26.41	1.71	0.316	0.27	1.006

3-dimensional disturbances

$\langle R\rangle_{H_2O}$	l (cm)	c (cm/s)	$2\pi/\nu\alpha$ (cm)	$2\pi/\beta$ (cm)	$\alpha\mu_R/\alpha c$	δ	α_s
7.32	0.961	15.34	1.92	1.138	0.126	0.062	0.675
11.42	0.848	18.42	1.70	1.38	0.186	0.10	0.783
16.40	0.819	21.30	1.64	1.71	0.238	0.15	0.868
21.10	0.764	23.60	1.53	2.49	0.247	0.20	0.928
27.16	0.742	26.37	1.48	2.97	0.334	0.27	0.984

Kapitza's prediction

$\langle R\rangle_{H_2O}$	l (cm)	c (cm/s)	δ	α_2
7.36	0.882	15.39	0.062	0.724
11.46	0.763	18.71	0.10	0.874
16.51	0.710	21.81	0.15	0.971
21.21	0.693	24.2	0.20	1.025
27.4	0.621	27.7	0.27	1.173

TABLE 5. Most stable member of the γ_1 family

last unstable wave at α_s is slightly above α_m and it is dominated by three-dimensional disturbances with small β and $\nu = 0.5$. The stationary waves near α_s remain unstable to sideband ($\nu \ll 1$) and subharmonic ($\nu = 0.5$) two-dimensional disturbances with growth rates close to but smaller than the three-dimensional ones. In fact, the wave least unstable to two-dimensional disturbances has a wavenumber α_2 only slightly higher than α_s. The growth rate of the dominant disturbance at α_s is two to four times smaller than the dominant growth rate of the flat film (which is equivalent to that of the solitary wave at $\alpha = 0$ in figure 12). This implies that the lifetime or length of the selected stationary wave is two to four times that of the flat inception region, which is already quite visible in a channel. The dominant growth rate of the stationary waves at α_s increases with δ. For δ in excess of unity, it is of the same order as the dominant flat-film growth rate. Beyond that ($\delta \gtrsim 1$), one does not expect the wave evolution to be locally stationary. Another requirement for the stationary assumption to hold is timescale separation that stipulates that the unstable disturbances must have a far smaller absolute value than the stable ones. This is related to the argument that the evolution involves two timescales which are used in the Stuart–Landau formalism and the Center Manifold theories (Cheng & Chang 1990). For all our computed results, only one or two eigenvalues are unstable near α_s and their growth rates are at least 5 times larger than the growth rate of the most stable mode. The results for the γ_1 family are also tabulated in table 5 and compared to Kapitza's prediction (27*a*). It is clear that the latter is an extremely accurate estimate of the stability of the stationary waves to two-dimensional disturbances at small δ. The wave in γ_1 with the highest flow rate is also predicted to the third decimal place by Kapitza's criterion in table 5, confirming the ability of (27*a*) to predict α_2 to within 10% for $\delta < 0.20$. The dissipation rate $\dot{E}$ is shown in figure 13 for $\delta = 0.062$. A single minimum close to α_2 is seen. The location of α_s is also marked in figure 8. It is clear that this selected wave is slower and shorter

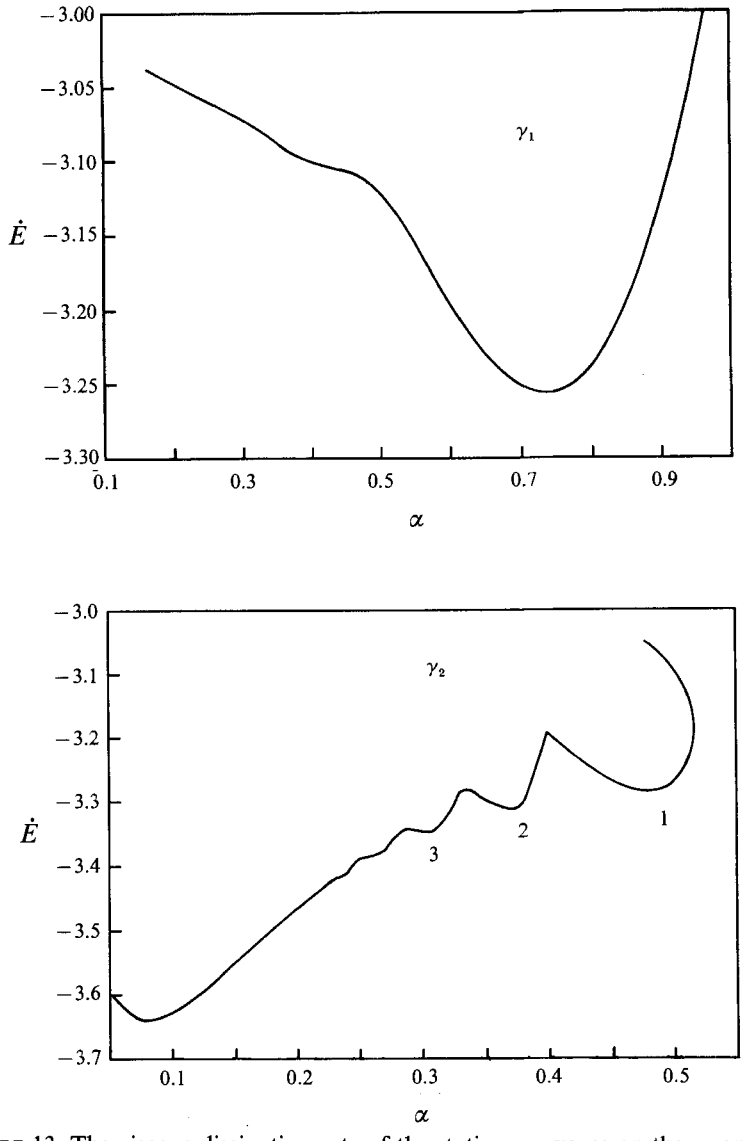

FIGURE 13. The viscous dissipation rate of the stationary waves on the γ_1 and γ_2 families at $\delta = 0.062$. The local minima for the γ_2 family are also listed in table 6.

than the fastest growing wave at inception with wavenumber α_m. In figure 14, we compare the inception speed data of Stainthorp & Allen (1965) and the γ_1 stationary wave speed data from naturally excited experiments of Stainthorp & Allen and Kapitza & Kapitza (1949) to the predicted speed from the linear dispersion relationship at α_m and the speed of the stationary wave at α_s. It is clear that, while both sets of speed data from Stainthorp & Allen are above the predicted values, a statistically significant separation exists between them and the γ_1 stationary waves of Kapitza & Kapitza possess wave speeds close to our prediction.

Typical growth rates of the dominant two-dimensional disturbances for the γ_2 family are shown in figure 15. The growth rate again approaches those of the flat-film Nusselt basic state at the solitary limit $\alpha \to 0$. The shorter waves remain unstable to sideband

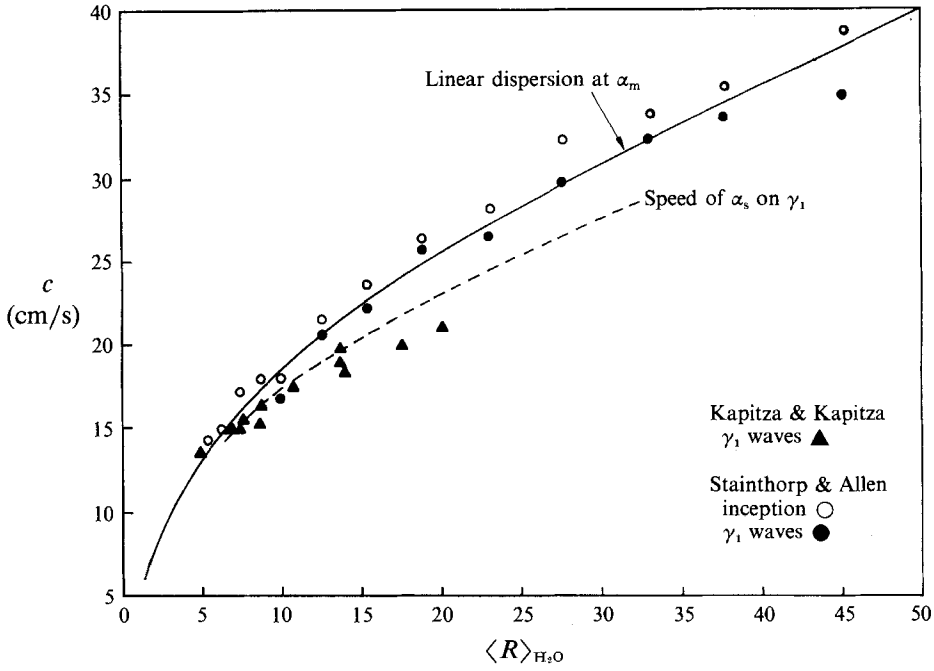

FIGURE 14. Difference in wave speeds in the inception region and in the finite-amplitude capillary wave region corresponding to the γ_1 wave family.

and subharmonic instabilities. However, in the intermediate region, multiple discrete regions of stability are seen. The distance between these intervals decreases with decreasing α. There exists a limiting stable interval with a lowest interval of α, centered at α_f. This lower bound decreases with increasing δ. This is in contrast with the growth rates of the γ_1 family where all waves are unstable to two-dimensional disturbances for $\delta > 0.037$ and there exists a unique minimum of the two-dimensional growth rate. In all these discrete intervals of stability, the waves are unstable to three-dimensional disturbances with a very small growth rate, which is not shown in figure 15. Outside the stable intervals, two-dimensional disturbances and, within the intervals, the small but dominant three-dimensional disturbances have long transverse variation ($\beta \ll 1$) and subharmonic ($\nu = 0.5$) or sideband ($\nu \ll 1$) streamwise variations. As δ increases, the growth rate of the γ_2 family tends to increase as a whole with the shorter waves destabilizing more than the longer waves. As a result, some of the stable intervals at higher α disappear with increasing δ. The stable intervals at lower α also shrink in size such that they can be accurately represented by a single value of α. For example, the interval with the longest stable waves on γ_2 corresponds to a small gap around α_f. We will hence represent these intervals by the discrete wavenumbers at their centres. Kapitza's dissipation selection theory is again extremely accurate for the γ_2 family at low δ as seen in figure 13 and table 6. The centres of the stable intervals appear as local minima in the dissipation and several of them are accurately captured. Comparing to the dissipation rate of the γ_1 family, it appears that a global minimum of the dissipation rate exists and it corresponds to the lower accumulation point α_f of the stable intervals before the growth rate approaches the flat-film limit of the solitary waves. At this small value of α_f, the waves resemble solitary waves with the large tear-drop hump occupying only about one-fourth or one-fifth of the entire wavelength. The remaining portion is

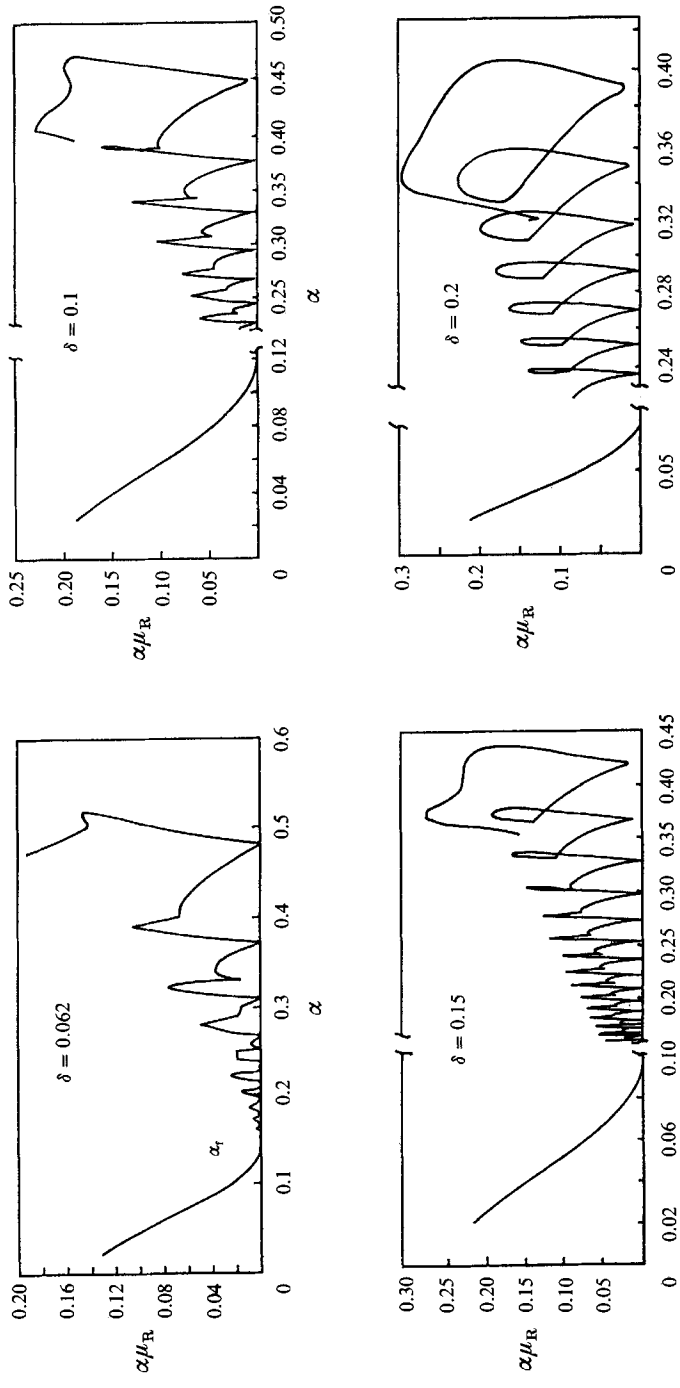

FIGURE 15. Typical computed growth rates of the dominant two-dimensional disturbances of the γ_2 family at $\delta = 0.062$, 0.1, 0.15 and 0.2.

	Two-dimensional linear stability		Kapitza's criteria	
$\langle R\rangle_{H_2O}$	l (cm)	c (cm/s)	l (cm)	c (cm/s)
7.42	1.33	17.4	(1) 1.33	17.4
7.49	1.71	18.6	(2) 1.72	18.6
7.57	2.06	19.6	(3) 2.11	19.7
7.65	2.37	20.5	Absent	—
8.07	4.51	25.2	(4) 7.83	29.5

TABLE 6. Selected wave members on γ_2 at $\delta = 0.062$

covered by small to imperceptible capillary waves. Nevertheless, these capillary waves must provide sufficient interaction to suppress the flat-film instability of a true solitary wave. At higher δ, the capillary waves are larger and their stronger interaction can then sustain a larger separation between the humps. The conclusion that the near-solitary wave at α_f is the global minimum of all stationary waves is, of course, only true at low δ. At higher δ values, inertia and surface tension effects must be considered. The stable intervals of the γ_2 family of water are shown in figure 16. As δ (or $\langle R\rangle$) increases, some of the shorter waves begin to destabilize and the longer stable waves begin to disappear as minima in Kapitza's dissipation rate. The implied conclusion that the long waves near α_f are unstable at large δ is, however, erroneous since our linear stability result indicates that they remain stable. Hence, interaction between the capillary waves, which can involve the capillary or inertia forces ignored in the dissipation theory, remains stabilizing. The stable intervals are also sketched in figure 8. We have also investigated the stability of the $\gamma_2^{(n)}$ families and found them to all be unstable to two-dimensional disturbances. They hence will probably not be selected under sufficiently rich excitation.

An intriguing qualitative explanation for the multiple intervals of long γ_2 waves that are stable to two-dimensional disturbances is offered by the coherent structure theory for solitary wave interaction (Elphick, Meron & Spiegel 1988). One notices on examining figure 7 that the long periodic waves on γ_2 can be accurately approximated by separating the same solitary wave structure at vanishing α by different intervals. (The wave tracings in figure 7 are normalized by their wavelengths and this observation hence requires some care.) Consequently, even though the true solitary wave is unstable because of the large span of flat films away from its coherent structure (a tear-drop hump preceded by front-running capillary 'bow' waves), which occupies a relatively small interval of space, the same coherent structure can be placed in a periodic train to yield a stable periodic wave. We again demonstrate this concept with the simple KS equation (20) even though the stable waves appear only at finite δ. Let us approximate $H(\xi,\tau)$ by

$$H(\xi,\tau) = U_i(\xi_i) + \sum_{k\neq i} U_k(\xi_k), \tag{30}$$

where U_i is a solitary wave solution satisfying either (21) and (22) or (23), depending on the formulation. The function U_k represents the other solitary wave coherent structures which have identical shapes but different locations and possibly different speeds. The local coordinates $\xi_i = \xi - \int c_i(\tau)\,d\tau$ have origins at the maxima of the ith solitary wave which moves at speed c_i. (Since (20) has been properly reduced, its solitary wave solution approaches zero at both infinities and (30) does not require base-line corrections.) We shall only be interested in the interaction of the ith solitary wave

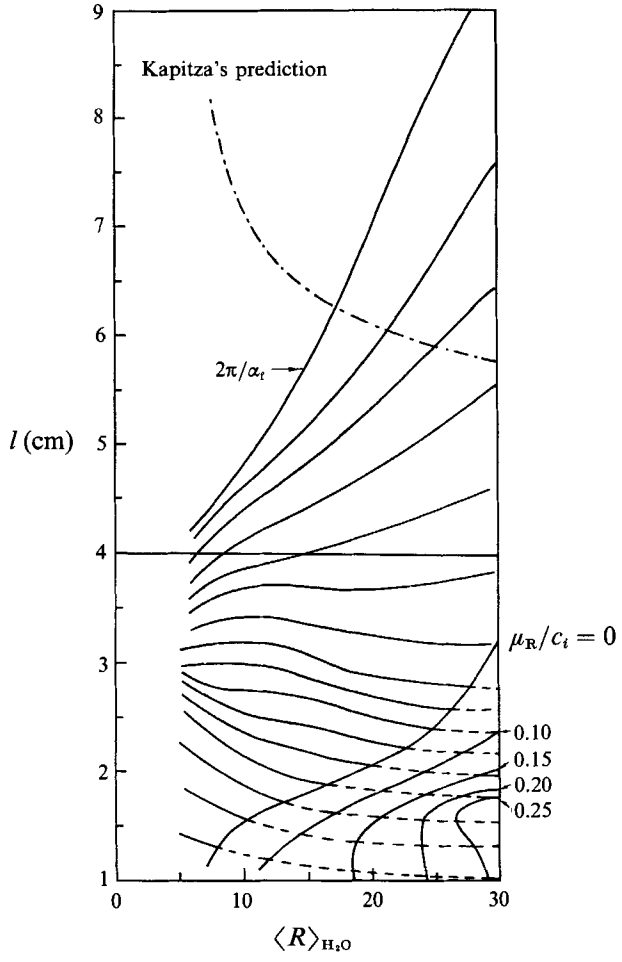

FIGURE 16. The predicted stable waves on the γ_2 family for water. The shorter ones destabilize at higher Reynolds numbers. The longer ones are very robust in spite of Kapitza's prediction of eventual destabilization at high Reynolds numbers.

with its two nearest neighbours, namely $k = i-1$ and $i+1$. The solitary waves are also assumed to be sufficiently apart such that the interaction occurs only at the small-amplitude ends of the solitary waves, which can be described by (Chang 1986)

$$U_f \sim A\,e^{-\sigma_1 \xi}\cos(\omega\xi + \phi_0), \tag{31a}$$

$$U_b \sim B e^{\sigma_2 \xi} \tag{31b}$$

where A, B and ϕ_0 are positive constants that must be obtained from the full solitary wave solution of figure 2, but σ_i and ω can be easily determined from the linearized version of (21) or (23). Equation (31*a*) for the front end describes the front-running capillary waves. Knowing that μ approaches 1.2 from figure 2 and inserting $H \sim e^{\sigma\xi}$ into the linearized version of (21), one obtains the eigenvalue problem

$$\sigma^3 + \sigma - 1.2 = 0, \tag{32}$$

which yields $\sigma_1 = 0.38$, $\omega = 1.20$ and $\sigma_2 = 0.76$.

Multiplying (20) by H and integrating from $\xi = -\infty$ to $\xi = +\infty$ yields an evolution equation for the deviation flux Q:

$$\tfrac{1}{2}(\mathrm{d}/\mathrm{d}t)\langle H^2\rangle = \langle H_\xi^2\rangle - \langle H_{\xi\xi}^2\rangle. \tag{33}$$

Inserting (30) into (33) and retaining only the leading-order mutual interaction terms (all self-interaction terms vanish by definition), one obtains

$$\begin{aligned}\frac{1}{2}\frac{\mathrm{d}}{\mathrm{d}t}\langle H^2\rangle &= 2\sum_{k\neq i}\left\langle \frac{\partial U_i}{\partial \xi_i}\frac{\partial U_k}{\partial \xi_k} - \frac{\partial^2 U_i}{\partial \xi_i^2}\frac{\partial^2 U_k}{\partial \xi_k^2}\right\rangle \\ &= 2\sum_{k\neq i}\left\langle [\mu U_i - 2U_i^2]\frac{\partial U_k}{\partial \xi_k}\right\rangle,\end{aligned} \tag{34}$$

where (21) has been invoked after integration by parts.

The excess flux of a stationary periodic train of solitary waves does not vary in time, $(\mathrm{d}/\mathrm{d}t)\langle H^2\rangle = 0$, and the separation between the solitary waves is constant at s,

$$\xi_{i-1} = \xi_i + s, \quad \xi_{i+1} = \xi_i - s. \tag{35a, b}$$

Equation (34) can then be rewritten for a periodic wave as

$$\begin{aligned}&\langle [\mu U_i - 2U_i^2]\, A(-\sigma_1 + \mathrm{i}\omega)\exp(-\sigma_1 + \mathrm{i}\omega)\,\xi\rangle \exp\{(-\sigma_1 + \mathrm{i}\omega)s + \mathrm{i}\phi_0\} + \text{c.c.} \\ &\quad + \langle [\mu U_i - 2U_i^2]\, B\sigma_2 \exp(\sigma_2 \xi)\rangle \exp(-\sigma_2 s) \equiv F(s) = 0,\end{aligned} \tag{36}$$

where c.c. denotes complex conjugate.

The zeros of $F(s)$ are hence the wavelengths of stationary periodic waves and as in Elphick *et al.* (1988), the stable periodic waves form a subset of these zeros. We shall refrain from an exact evaluation of the necessary integrals in (36) here but observe that in the long wave limit, $s \to \infty$, $F(s)$ oscillates about zero with a frequency ω corresponding to the wave frequency ω of the front-running capillary waves. Consequently, an infinite number of equally spaced zeros at large s,

$$\lim_{n\to\infty} s_n = 2\pi n/\omega. \tag{37}$$

(There is another subset corresponding to $n\pi/\omega$ but these correspond to unstable periodic waves.) Equivalently, (37) predicts that the wavenumber α_n of the long stable waves on γ_2 varies as n^{-1},

$$\alpha_n \sim \omega/n \tag{38a}$$

and the interval between the stable waves varies as n^{-2},

$$\Delta\alpha_n = \alpha_n - \alpha_{n-1} \sim \omega n^{-2}. \tag{38b}$$

Both predictions are consistent with our linear stability results of figure 15. For example, for $\delta = 0.062$, the stable waves are located at approximately $\alpha = (0.48, 0.38, 0.31, 0.26, \ldots)$. This yields an s_n of approximately $13 + 3.8n$, after invoking the lengthscale of the KS equation $\xi = \alpha_0 x = (18\delta)^{\frac{1}{2}}x$, which is close to the $5.2n$ prediction of (37). The variations of α_n and $\Delta\alpha_n$ for all δ in figure 15 are also close to the predictions of (38).

The above theory only measures the interaction among the nearest coherent structures in a train of solitary waves. It ignores the primary instability of a flat film when the solitary waves are too far apart. Consequently, the series α_n of (38) does not approach zero in figure 15. Instead, below α_f, the neglected primary instability of the flat film begins to dominate and destabilizes all waves with wavelengths longer than

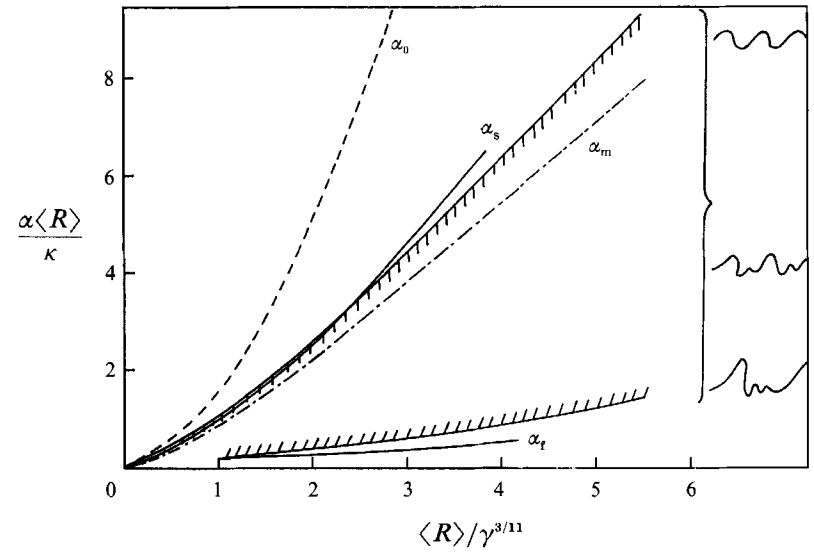

FIGURE 17. The shaded curves are bounds on the wavenumbers of the observed waves in the forced experiment of Alekseenko *et al.* (1985) for water. They are favourably compared to our predictions of α_s and α_f.

$2\pi/\alpha_f$. Strong coherent-structure interaction reduces this flat-film primary instability and hence lowers α_f. This explains the decrease in α_f with increasing δ since the solitary wave amplitude increases with δ. It may also explain an apparent inconsistency of the coherent-structure theory. Owing to symmetry (25), the theory can also be applied to the γ_1 (actually C_{-1}) family of the KS equation to yield the conclusion that the negative solitary wave of figure 6 can also interact favourably to form a stable periodic train. This stability is not found in long-wave members of the γ_1 family. This is probably due to the far smaller (and slower in absolute speed) solitary wave limit of the γ_1 family relative to the γ_2 family evident in figures 7 and 8. These weak solitary waves of γ_1 simply cannot overwhelm the flat-film instability of long periodic stationary waves. This is evident in the growth rates of the γ_1 family in figure 12. The flat-film instability begins to dominate at a relatively high $\alpha(< 0.6)$ compared to $\alpha_f(< 0.2)$ of the γ_2 family. This argument also explains why the C_1 family of the KS equation is found to be unstable. The positive solitary waves at vanishing δ are also too weak to sustain a periodic train. The stable intervals hence exist at small but finite δ on the γ_2 family because of the dramatic increase in amplitude and speed of the γ_2 solitary wave with respect to δ. Finally, in spite of the surprising accuracy of (38) in the above theory, it must be remembered that the theory remains speculative since the KS equation invoked in the analysis does not yield stable periodic waves near the solitary-wave limit. The only stable waves of the KS equation lie within the near-neutral wavenumber band $(\alpha/\alpha_0) \in (0.77, 0.84)$ on the S family. The dispersive effect of δ somehow validates the above coherent structure theory. A more detailed theory which includes δ will appear elsewhere (Chang *et al.* 1993).

A selection mechanism has now appeared from our analysis. As is sketched in figure 8, an unforced system with minimal three-dimensional disturbance will appear as two-dimensional monochromatic waves with wavenumber α_m after the inception region. It should then approach finite-amplitude capillary waves on γ_1 with wavenumbers close to α_s or α_2 (path I) and then near solitary waves close to α_f on γ_2 (path II). The second

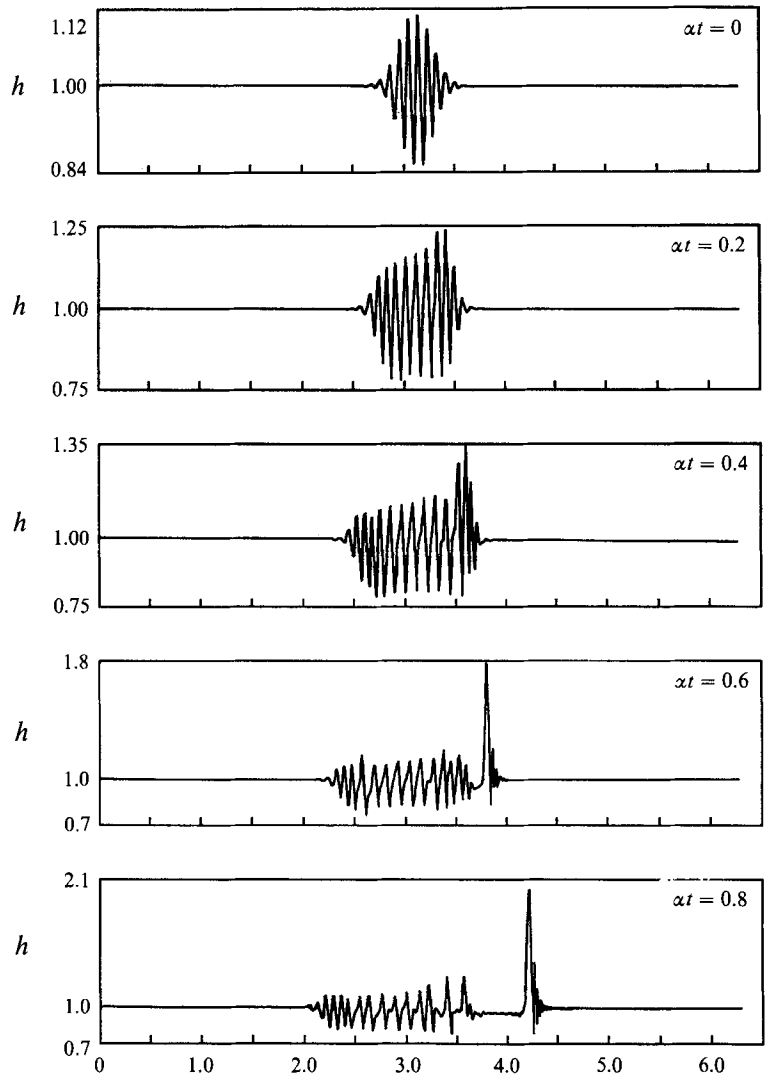

FIGURE 18. Evolution simulation in the Lagrangian frame with speed 3 at $\delta = 0.05$. An initial packet with a local wave number equal to $\alpha_m = 0.612$ is introduced. Slower waves with shorter wavelengths corresponding to α_2 on γ_1 are seen to fall back from the wave packet during path I of figure 8. This is followed by the creation of long solitary waves near α_f on the γ_2 family which separates from the packet during path II of the transition. The spatial coordinate is αx where $\alpha = 0.00897$.

transition from γ_1 to γ_2 can be a subharmonic instability if the suppressed three-dimensional disturbances have grown to a significant amplitude. In this case, a stable wave on γ_2 with a wavenumber approximately half that of α_s will be approached. If the disturbances remain two-dimensional, the dominant two-dimensional disturbance on γ_1 is either a sideband instability ($\nu \ll 1$) or a subharmonic instability ($\nu = 0.5$) and a long stable wave on γ_2 near α_f may also be selected. Further downstream, these near-solitary waves on γ_2 will eventually succumb to long transverse variations.

If periodic forcing with two-dimensional disturbance is introduced, any of the stable waves on γ_2 can be observed since the initial transitions (paths I and II) have been suppressed. If the forcing frequency is higher than the shortest stable wave of γ_2, then

the waves will most likely evolve towards α_s or α_2 on γ_1 before undergoing transitions to the long waves on γ_2 as in a naturally excited system. This would then imply that the observed waves for a forced experiment are bounded between α_s and α_f. This was indeed reported by Alekseenko *et al.* (1985) and we favourably compare their experimental bound to α_s and α_f from our theory in figure 17.

Finally, we report a preliminary two-dimensional simulation that supports our theory on the wave evolution process. Simulation of wave evolution on a falling film is hampered by the exceedingly long evolution length of all the transitions. One solution is to carry out the simulation in a Lagrangian frame moving at a speed of 3 and to invoke periodic boundary conditions. To include several near-solitary waves in the domain, however, the spatial period of the computational box must still be large. Moreover, periodicity usually introduces non-stationary interaction among the waves that does not appear in the real system. We overcome these obstacles by ignoring the linear inception region and begin our simulation with a wave packet with the local wavenumber α_{loc} close to α_m in the middle of a computation box in the Lagrangian frame. The wave packet initial condition removes the boundary effects of the periodic boundary condition and it also minimizes the interaction between the γ_1 and γ_2 waves since they will propagate towards the flat films at two different ends of the wave packet. A total of 256 complex Fourier modes are used with a fourth-order Runge–Kutta time integration scheme with a step size of $\alpha\Delta t = 10^{-4}$. As seen in figure 18, one sees an initial approach towards a shorter and slower γ_1 capillary wave as these waves move toward the back of the packet. A secondary transition towards the near-solitary waves of γ_2 near α_f is then seen as the unique solitary wave shapes begin to evolve and separate from the front of the wave packet. Our simulations for $\delta < 0.037$ show that the second transition to γ_2 waves does not occur. This is, of course, due to the existence of waves stable to two-dimensional disturbances on γ_1 near α_2. Changing the width or amplitude of the initial wave packet does not alter the evolution process qualitatively. Reducing α_{loc} of the initial wave packet, however, can initiate a direct transition to the γ_2 family without approaching the stationary waves on γ_1. This then corresponds to slowly forced experiments that bypass the initial deceleration state (path I in figure 8) towards the γ_1 waves.

6. Summary

The primary, secondary and tertiary transitions of waves to the inception, capillary and solitary wave regimes on falling film have been analysed. There exist an infinite number of stationary wave families and all of them are unstable to three-dimensional disturbances. However, if three-dimensional disturbances are minimized, then several discrete members on two key wave families, γ_1 and γ_2, will have sufficient lifetimes to appear on the film. There is only one such wave α_s (or α_2 if three-dimensional disturbances are suppressed) on γ_1 and all naturally excited two-dimensional waves will evolve through this wave. There are several candidates on γ_2 and the particular one selected depends on the disturbances present at the end of the γ_1 capillary wave regime. If a purely two-dimensional wave is selected on γ_2, it will either be a stable wave with wavenumber close to $\frac{1}{2}\alpha_s$ or $\frac{1}{2}\alpha_2$ via a subharmonic transition or a long wave near α_f via a sideband transition. If three-dimensional disturbances are present, it will undergo a subharmonic transition in the streamwise direction with long transverse variation. It is known that after the solitary wave regime, the waves break into non-stationary three-dimensional patterns. This implies that three-dimensional stationary waves either do not exist or have very short lifetimes to be meaningful. This final transition to

interfacial 'turbulence' must then be analysed with an entirely different approach. Our suspicion is that an extension of the coherent theory to include long transverse phase instabilities should be most promising towards further understanding of this final transition.

This work is supported by DOE under the Engineering Research Programme.

Appendix A. Derivation of two-dimensional boundary-layer equations

After the scaling by κ, one obtains from (1)–(4), for the simplest case of $\theta = \frac{1}{2}\pi$,

$$\frac{\partial u}{\partial t}+u\frac{\partial u}{\partial x}+v\frac{\partial u}{\partial y}=-\frac{\partial p}{\partial x}+\frac{1}{R}\left(\frac{\partial^2 u}{\partial y^2}+3+\frac{1}{\kappa^2}\frac{\partial^2 u}{\partial x^2}\right),$$

$$\frac{1}{\kappa^2}\left(\frac{\partial v}{\partial t}+u\frac{\partial v}{\partial x}+v\frac{\partial v}{\partial y}\right)=-\frac{\partial p}{\partial y}+\frac{1}{\kappa R}\left(\frac{\partial^2 v}{\partial y^2}+\frac{1}{\kappa^2}\frac{\partial^2 v}{\partial x^2}\right),$$

$$\frac{\partial u}{\partial x}+\frac{\partial v}{\partial y}=0,$$

$$y=h(x,t)\colon\quad v=\frac{\partial h}{\partial t}+u\frac{\partial h}{\partial x},$$

$$p+\frac{W}{\kappa^2}\frac{h_{xx}}{(1+h_x^2/\kappa^2)^{\frac{3}{2}}}-\frac{2}{\kappa R}\frac{\partial v}{\partial y}\frac{1+h_x^2/\kappa^2}{1-h_x^2/\kappa^2}=p_0,$$

$$\frac{\partial u}{\partial y}+\frac{1}{\kappa^2}\frac{\partial v}{\partial x}+\frac{4h_x}{\kappa^2(1-h_x^2/\kappa^2)}\frac{\partial v}{\partial y}=0,$$

$$y=0\colon\quad u=v=0.$$

Reverting to the ϵ and δ notation of (8) and carrying out an expansion in ϵ, one obtains after rescaling p by $\delta, p\to p/\delta$,

$$\delta\left(\frac{\partial u}{\partial t}+u\frac{\partial u}{\partial x}+v\frac{\partial u}{\partial y}\right)+\frac{\partial p}{\partial x}-\frac{1}{15}\left(\frac{\partial^2 u}{\partial y^2}+3\right)=\epsilon\frac{\partial^2 u}{\partial x^2},$$

$$\frac{\partial p}{\partial y}=\epsilon\left[\frac{\partial^2 u}{\partial y^2}-15\delta\left(u\frac{\partial u}{\partial y}+\frac{\partial v}{\partial t}\right)\right],$$

$$\frac{\partial u}{\partial x}+\frac{\partial v}{\partial y}=0,$$

$$y=h(x,t)\colon\quad v=h_t+uh_x,$$

$$p+\tfrac{1}{5}h_{xx}-p_0=2\epsilon\left[\frac{9}{4}h_{xx}h_x^2+\frac{\partial v}{\partial y}-h_x\frac{\partial u}{\partial y}\right],$$

$$\frac{\partial u}{\partial y}=15\epsilon\left[h_x^2\frac{\partial u}{\partial y}-\frac{\partial v}{\partial x}-4h_x\frac{\partial v}{\partial y}\right].$$

To leading order in ϵ, $\partial p/\partial y$ vanishes, indicating that pressure is independent of the transverse direction, and $\partial p/\partial x$ in the x-momentum equation can then be determined from the normal stress condition at the interface, $p = p_0-\frac{1}{5}h_{xx}$. This yields equation (9).

Appendix B. Numerical technique for the stationary waves

At a particular streamwise location x, the values of u and v at the end of element k is labelled $(u_k, v_k), k = 1, 2, \ldots, N$, where $(u_0, v_0) = (0, 0)$ by (17*e*) and (17*f*) and the kth element spans from $y_{k-1} = (k-1)\,h(x)/N$ to $y_k = kh(x)/N$. We then integrate (17) from y_k to y_{k+1}:

$$\frac{\mathrm{d}}{\mathrm{d}x}\int_{y_k}^{y_{k+1}}(-cu+u^2)\,\mathrm{d}y+\left[\frac{k+1}{N}u_{k+1}(c-u_{k+1})-\frac{k}{N}u_k(c-u_k)\right]\frac{\mathrm{d}h}{\mathrm{d}x}+u_{k+1}v_{k+1}-u_k v_k$$
$$=\frac{1}{5\delta}\left(\frac{h}{N}\frac{\partial^3 h}{\partial x^3}+\frac{h}{N}+\frac{1}{3}\frac{\partial u_{k+1}}{\partial y}-\frac{1}{3}\frac{\partial u_k}{\partial y}\right), \quad \text{(B 1)}$$

$$v_{k+1}=v_k-\frac{\partial}{\partial x}\int_{y_k}^{y_{k+1}}u\,\mathrm{d}y+\left[\frac{k+1}{N}u_{k+1}-\frac{k}{N}u_k\right]\frac{\partial h}{\partial x}, \quad \text{(B 2)}$$

$$k=0,1,2,\ldots,N-1; \quad \text{and} \quad \int_0^1 u\,\mathrm{d}y-ch=q-c. \quad \text{(B 3)}$$

In deriving (B 3), (17) has been integrated in the vertical direction. Equations (B 1)–(B 3) are extremely difficult to integrate because the third derivative term $\partial^3 h/\partial x^3$ appears in every layer equation. We hence isolate the right-hand side of (B 1) by summing over all elements at every x to yield

$$\frac{\mathrm{d}}{\mathrm{d}x}\int_0^h(-cu+u^2)\,\mathrm{d}y=\frac{1}{5\delta}\left(h\frac{\partial^3 h}{\partial x^3}+h-\frac{1}{3}\frac{\partial u_0}{\partial y}\right). \quad \text{(B 4)}$$

The momentum balance equation (B 1) for each element is also replaced by the following equation which is obtained by subtracting the equation for k from the one for $k-1$:

$$\frac{\mathrm{d}}{\mathrm{d}x}(\tau_{k+1}-\tau_k)+\left[\frac{k+1}{N}u_{k+1}(c-u_{k+1})-\frac{2k}{N}u_k(c-u_k)+\frac{k-1}{N}u_{k-1}(c-u_{k-1})\right]\frac{\mathrm{d}h}{\mathrm{d}x}$$
$$+u_{k+1}v_{k+1}-2u_k v_k+u_{k-1}v_{k-1}=\frac{1}{15\delta}\left(\frac{\partial u_{k+1}}{\partial y}-2\frac{\partial u_k}{\partial y}+\frac{\partial u_{k-1}}{\partial y}\right), \quad \text{(B 5)}$$

where $k = 1, 2, \ldots, (N-1)$, and

$$\tau_k=\int_{h_{k-1}}^{h_k}(-cu+u^2)\,\mathrm{d}y.$$

This eliminates the destabilizing h_{xxx} term from each element. We also note that derivatives of v do not appear. The continuity and kinematic equations, (B 2) and (B 3), remain the same.

We shall use a second-order polynomial for u at every element,

$$u=u_k+\mathrm{D}u_k\,\eta_k+\tfrac{1}{2}\mathrm{D}^2u_k\,\eta_k^2=A_k(x)+B_k(x)\,\eta_k+\tfrac{1}{2}C_k(x)\,\eta_k^2,$$

where η_k is the local coordinate for layer k

$$\eta_k=N(y-y_k)/h$$

and $\mathrm{D}u_k$ and D^2u_k represent the first and second derivatives of u at y_k. A more elegant expansion with orthogonal polynomials like the Legendre basis is also possible. In such cases, (B 1) and (B 2) would involve inner products with some test functions, which

would be the same bases for a Galerkin formulation of the finite-element scheme. We shall ensure both the zeroth derivative and the first derivative are continuous at the layer boundaries:

$$u_k + \mathrm{D}u_k + \tfrac{1}{2}\mathrm{D}^2 u_k = u_{k+1}, \tag{B 6}$$

$$\mathrm{D}u_k + \mathrm{D}^2 u_k = \mathrm{D}u_{k+1}, \tag{B 7}$$

for $k = 0, 1, 2, \ldots, (N-1)$. We can combine both equations to eliminate $\mathrm{D}^2 u_k$,

$$u_k + \tfrac{1}{2}(\mathrm{D}u_{k+1} + \mathrm{D}u_k) = u_{k+1} \tag{B 8}$$

for $k = 0, 1, 2, \ldots, (N-1)$. For the last element, we impose the stress-free condition (17*d*),

$$\mathrm{D}u_N = 0. \tag{B 9}$$

That the first derivative is continuous, as is the zeroth derivative, allows us to use a very small number of elements although the number of equations increases. In (B 8) and (B 9), we have $N+1$ equations for the $N+1$ first derivatives of u at y_k $(\mathrm{D}u_0, \mathrm{D}u_1, \ldots, \mathrm{D}u_N)$. Since they are linear equations, one can obtain an explicit expression of the first derivatives in terms of the zeroth derivatives

$$\mathrm{D}u_k = f_k(u_1, u_2, \ldots, u_N).$$

Upon evaluating $\mathrm{D}u_k, \mathrm{D}^2 u_k$ can then be obtained from (6).

With the above treatment of the derivatives, (B 4), (B 5), (B 2) and (B 3) yield $2N+1$ equations for the unknowns $\{u_k, v_k, h\}_{k=1}^{N}$ at every x-location. Since v_k can be solved explicitly from (B 2) and u_N can be conveniently expressed as a function of $\{u_K\}_{k=1}^{N-1}$ and h with (B 3), it is simpler to view (B 4) and (B 5) as N equations for the N unknowns $\{u_k\}_{k=1}^{N-1}$ and h. We now seek resolution in the x-direction. A Fourier series expansion is used in this direction:

$$h = 1 + \sum_{m=1}^{M} a_m \cos \alpha m x + b_m \sin \alpha m x, \tag{B 10}$$

$$u_k = A_k^{(0)} + \sum_{m=1}^{M} A_k^{(m)} \cos \alpha m x + B_k^{(m)} \sin \alpha m x, \tag{B 11}$$

where α is the wavenumber $2\pi/l$. Without loss of generality, we can choose a_1 to be zero which corresponds to an arbitrary assignment of a reference point. Substituting (B 10) and (B 11) and equating terms of the same harmonic, we then have a total of $(2M+1)(N+1)$ unknowns in c, q, $\{a_m\}_{m=2}^{M}$, $\{b_m\}_{m=1}^{M}$, $\{A_k^{(m)}\}_{m=0}^{M}$ and $\{B_k^{(m)}\}_{m=1}^{M}$ and the same number of equations. We solve this system of quadratic equations with a Newton iteration method. Without the h_{xxx} curvature term and with the layer decomposition, the inverted matrix in the iteration has a very narrow band. Convergence with respect to both N and M are tested. Less than 0.5% error in the largest Fourier coefficient of h is ensured. The maximum N is 7 and the maximum M is about 70, to yield a total maximum of about 1000 equations and unknowns. The large $M_{\max}$ is because of the large Fourier contents of long solitary waves. The small $N_{\max}$ is due to our elimination of h_{xxx} at the interior elements and the imposition of continuous first derivative. Without these simplifications, $N_{\max}$ increases dramatically since the velocity profile can be highly non-parabolic. We calculate the nonlinear terms in the physical space and then insert them with the linear terms during the iteration in the Fourier space with the aid of a fast Fourier transform. This technique of solving equations of instability–dissipation type has the following advantage. The high-frequency (wavenumber) error generated during the evaluation of the nonlinear terms is damped during the

iteration in the Fourier space since the high-frequency modes are linearly stable as the iteration is quite analogous to the actual evolution in time. It hence accurately estimates the two dominant mechanisms in stationary waves – linear instability and nonlinear saturation. A continuation scheme is also used to trace the solution branches as a function of α. A typical wave profile requires 30 seconds on the CONVEX computer.

REFERENCES

ARMBRUSTER, D., GUCKENHEIMER, J. & HOLMES, P. 1988 Heteroclinic cycles and modulated travelling waves in systems with O(2) symmetry. *Physica* **29D**, 257–282.

ALEKSEENKO, S. V., NAKORYAKOV, V. E. & POKUSAEV, B. G. 1985 Wave formation on a vertical falling liquid film. *AIChE J.* **31**, 1446–1460.

BACH, P. & VILLADSEN, J. 1984 Simulation of the vertical flow of a thin wavy film using a finite element method. *Intl J. Heat Mass Transfer* **27**, 815–827.

BENJAMIN, T. B. 1957 Wave formation in laminar flow down an incline plane. *J. Fluid Mech.* **2**, 554–574.

BENNEY, B. J. 1966 Long waves in liquid films. *J. Math. Phys.* **45**, 150–155.

BRAUNER, H. & MARON, D. M. 1983 Modeling of wavy flow inclined thin films. *Chem. Engng Sci.* **38**, 775–788.

BUNOV, A. V., DEMEKHIN, E. A. & SHKADOV, V. YA 1984 On the non-uniqueness of nonlinear wave solutions in a viscous layer. *Prikh. Mat. Mekh.* **48**, 691–696.

CHANG, H.-C. 1986 Traveling waves in fluid interfaces: Normal form analysis of the Kuramoto–Sivashinsky equation. *Phys. Fluids* **29**, 3142–3147.

CHANG, H.-C. 1989 Onset of nonlinear waves on falling films. *Phys. Fluids* A **1**, 1314–1327.

CHANG, H.-C., DEMEKHIN, E. A. & KOPELEVICH, D. I. 1993 Laminarizing effects of dispersion in an active-dissipative nonlinear medium. *Physica D* (in press).

CHENG, M. & CHANG, H.-C. 1990 A generalized sideband stability theory via center manifold projection. *Phys. Fluids* A **2**, 1364–1379.

CHENG, M. & CHANG, H.-C. 1992*a* Stability of axisymmetric waves on liquid films flowing down a vertical column to azimuthal and streamwise disturbances. *Chem. Engng Commun.* **118**, 327–340.

CHENG, M. & CHANG, H.-C. 1992*b* Subharmonic instabilities of finite-amplitude monochromatic waves. *Phys. Fluids* A **4**, 505–523.

DEMEKHIN, E. A. 1983 Bifurcation of the solution to the problem of steady traveling waves in a layer of viscous liquid on an inclined plane. *Izv. Akad. Nauk SSSR Mekh. Zhidk i Gaza* **5**, 36–44.

DEMEKHIN, E. A., DEMEKHIN, I. A. & SHKADOV, V. YA 1983 Solitons in flowing layer of a viscous fluid. *Izv. Akad. Nauk SSSR, Mekh Zhid i Gaza* **4**, 9–16.

DEMEKHIN, E. A. & KAPLAN, M. A. 1989 Stability of stationary traveling waves on the surface of a vertical film of viscous fluid. *Izv. Akad. Nauk SSSR, Mekh. Zhidk. i Gaza* **3**, 34–41.

DEMEKHIN, E. A. & SHKADOV, V. YA 1985 Two-dimensional wave regimes of a thin liquid films. *Izv. Akad. Nauk SSSR, Mekh. Zhidk i Gaza* **3**, 63–67.

DEMEKHIN, E. A. & SHKADOV, V. YA 1986 Theory of solitons in systems with dissipation. *Izv. Akad. Nauk SSSR, Mekh. Zhidk i Gaza* **3**, 91–97.

DEMEKHIN, E. A., TOKAREV, G. YU & SHKADOV, V. YA 1991 Hierarchy of bifurcations of space-periodic structures in a nonlinear model of active dissipative media. *Physica D* **52**, 338–361.

ELPHICK, C., MERON, E. & SPIEGEL, E. A. 1988 Spatiotemporal complexity in traveling patterns. *Phys. Rev. Lett.* **61**, 496–499.

FUJIMURA, K. 1991 Method of center manifold and multiple scales for weakly nonlinear stability of fluid motions. *Proc. R. Soc. Lond.* A **434**, 719–733.

GJEVIK, B. 1970 Occurrence of finite-amplitude surface waves on falling liquid films. *Phys. Fluids* **13**, 1918–1925.

GLENDINNING, P. & SPARROW, C. 1984 Local and global behavior near homoclinic orbits. *J. Statist. Phys.* **35**, 645–696.

HO, L.-W. & PATERA, A. T. 1990 A Legendre spectral element method for simulation of unsteady incompressible viscous free-surface flow. *Comput. Meth. Appl. Mech. Engng* **80**, 355–366.

HWANG, S.-H. & CHANG, H.-C. 1987 Turbulent and inertial roll waves in inclined film flow. *Phys. Fluids* **30**, 1259–1268.

JOO, S. W., DAVIS, S. H. & BANKOFF, S. G. 1991 Long-wave instabilities of heated falling films: two-dimensional theory of uniform layers. *J. Fluid Mech.* **230**, 117–146.

KAPITZA, P. L. 1948 Wave flow of thin viscous fluid layers. *Zh. Eksp. Teor. Fiz.* **18**, 1, 3–28; also in *Collected Works*, Pergamon (1965).

KAPITZA, P. L. & KAPITZA, S. P. 1949 Wave flow of thin fluid layers of liquid. *Zh. Eksp. Teor. Fiz.* **19**, 105–120; also in *Collected Works*, Pergamon (1965).

KEVREKIDES, I., NICOLAENKO, B. & SCOVEL, J. C. 1990 Back in the saddle again: a computer-assisted study of the Kuramoto–Sivashinskey equation. *SIAM J. Appl. Maths* **50**, 760–790.

KHESHGI, H. A. & SCRIVEN, L. E. 1987 Disturbed film flow on a vertical plate. *Phys. Fluids* **30**, 990–997.

LIN, S. P. 1974 Finite amplitude side-band stability of a viscous film. *J. Fluid Mech.* **63**, 417–429.

LIN, S. P. 1983 In *Film Waves on Fluid Interfaces* (ed. R. E. Meyer), pp. 261–290. Academic.

NAKAYA, C. 1975 Long waves on thin fluid layer flowing down an incline plane. *Phys. Fluids* **18**, 1407–1412.

NAKORYAKOV, V. E., POKUSAEV, B. G. & RADEV, K. B. 1985 Influence of waves on convective gas diffusion in a falling down liquid film. In *Hydrodynamics and Heat and Mass Transfer of Free-Surface Flows*, pp. 5–32. Institute of Heat Physics, Siberian Branch of the USSR Academy of Science, Novosibirsk, (in Russian).

NEPOMNYASCHY, A. A. 1974 Stability of wave regimes in a film flowing down an inclined plane. *Izv. Akad. Nauk SSSR, Mekh. Zhidk i Gaza* **3**, 28–34.

PIERSON, F. W. & WHITAKER, S. 1977 Some theoretical and experimental observation of wave structure of falling liquid films. *Ind. Engng Chem. Fundam.* **16**, 401–408.

PROKOPIOU, TH. CHENG, M. & CHANG, H.-C. 1991 Long waves on inclined films at high Reynolds number. *J. Fluid Mech.* **222**, 665–691.

PUGH, J. D. & SAFFMAN, P. G. 1988 Two-dimensional superharmonic stability of finite-amplitude waves in plane Poiseuille flow. *J. Fluid Mech.* **194**, 295–307.

PUMIR, A., MANNEVILLE, P. & POMEAU, Y. 1983 On solitary waves running down an inclined plane. *J. Fluid Mech.* **135**, 27–50.

SHKADOV, V. YA 1967 Wave conditions in the flow of thin layer of a viscous liquid under the action of gravity. *Izv. Akad. Nauk SSSR, Mekh. Zhidk i Gaza* **1**, 43–50.

SHKADOV, V. YA 1968 Theory of wave flows of a thin layer of a viscous liquid. *Izv. Akad. Nauk SSSR, Mekh. Zhidk i Gaza* **2**, 20.

SHKADOV, V. YA 1973 *Some Methods and problems of the Theory of Hydrodynamic Stability*. Moscow: Izd. MGU (in Russian).

STAINTHORP, F. P. & ALLEN, J. M. 1965 The development of ripples on the surface of liquid film flowing inside a vertical tube. *Trans. Inst. Chem. Engrs* **43**, 85–91.

TOUGOU, H. 1981 Deformation of supercritical stable waves on a viscous liquid film down an inclined wall with the decrease of wave numbers. *J. Phys. Soc. Japan* **50**, 1017–1024.

TRIFONOV, YU YA & TSVELODUB, O. YU 1985 Nonlinear waves on the surface of liquid films flowing down vertical wall. *Zh. Prikl. Mekh. Tekhn. Fiz.* **5**, 15–19.

TRIFONOV, YU YA & TSVELODUB, O. YU 1991 Nonlinear waves on the surface of a falling liquid film. *J. Fluid Mech.* **229**, 531–554.

TSVELODUB, O. YU 1980 Steady traveling waves on a vertical film of fluid. *Izv. Akad. Nauk SSSR, Mekh. Zhidk i Gaza* **4**, 142–146.

TSVELODUB, O. YU & TRIFONOV, YU YA 1989 On steady-state travelling solutions of an evolution equation describing the behavior of disturbances in an active dissipative media. *Physica D* **39**, 336–351.

TUCK, E. O. 1983 Continuous coating with gravity and jet stripping. *Phys. Fluids* **26**, 2352–2358.

YIH, C.-S. 1963 Stability of liquid flow down an inclined plane. *Phys. Fluids* **6**, 321–334.